Total mass density slopes of early-type galaxies using Jeans dynamical modelling at redshifts $0.29 < z < 0.55$

Caro Derkenne,[1,2]★ Richard M. McDermid,[1,2] Adriano Poci ⓘ,[1,3] Rhea-Silvia Remus,[4] Inger Jørgensen[5] and Eric Emsellem[6,7]

[1]*Research Centre for Astronomy, Astrophysics, and Astrophotonics, Department of Physics and Astronomy, Macquarie University, NSW 2109, Sydney, Australia*
[2]*ARC Centre of Excellence for All Sky Astrophysics in 3 Dimensions (ASTRO 3D), Australia*
[3]*Centre for Extragalactic Astronomy, University of Durham, Stockton Road, Durham DH1 3LE, UK*
[4]*Fakultät für Physik, Universitäts-Sternwarte München, LMU München, Scheinerstr 1, D-81679 München, Germany*
[5]*NSF's NOIRLab, 670 N. A'ohoku Place, Hilo, HI 96720, USA*
[6]*European Southern Observatory, Karl-Schwarzschild-Str 2, D-85748 Garching, Germany*
[7]*Centre de Recherche Astrophysique de Lyon UMR5574, CNRS, ENS de Lyon, Univ. Lyon, Univ. Lyon 1, F-69230 Saint-Genis-Laval, France*

ABSTRACT

The change of the total mass density slope, γ, of early-type galaxies through cosmic time is a probe of evolutionary pathways. Hydrodynamical cosmological simulations show that at high redshifts density profiles of early-type galaxies were on average steep ($\gamma \sim -3$). As redshift approaches zero, gas-poor mergers progressively cause the total mass density slope to approach the 'isothermal' slope of $\gamma \sim -2$. Simulations therefore predict steep density slopes at high redshifts, with little to no evolution in density slopes below $z \sim 1$. Gravitational lensing results in the same redshift range find the opposite, namely a significant trend of shallow density slopes at high redshifts, becoming steeper as redshift approaches zero. Gravitational lensing results indicate a different evolutionary mechanism for early-type galaxies than dry merging, such as continued gas accretion or off-axis mergers. At redshift zero, isothermal solutions are obtained by both simulations and dynamical modelling. This work applies the Jeans dynamical modelling technique to observations of galaxies at intermediate redshifts ($0.29 < z < 0.55$) in order to derive density slopes to address the tension between observations and simulations. We combine two-dimensional kinematic fields from Multi Unit Spectroscopic Explorer data with *Hubble Space Telescope* photometry. The density slopes of 90 early-type galaxies from the Frontier Fields project are presented. The total sample has a median of $\gamma = -2.11 \pm 0.03$ (standard error), in agreement with dynamical modelling studies at redshift zero. The lack of evolution in total density slopes in the past 4–6 Gyr supports a dry merging model for early-type galaxy evolution.

Key words: galaxies: evolution – galaxies: kinematics and dynamics.

1 INTRODUCTION

Studies of early-type galaxies are particularly informative for testing predictions of galaxy evolution models. Early-type galaxies are composed of old, passive stellar populations, representing the end product of many of the key processes of galaxy formation and evolution, such as star formation quenching, mergers, and accretion events (Conselice 2014). More pragmatically, they are also massive, have relatively high surface brightness, and are generally free of dust, allowing for easy observations even at high redshifts.

The mass assembly of early-type galaxies across cosmic time is a combination of the accretion of stars and the accretion of gas. Each process leaves a fingerprint on the structure and dynamics of the galaxy, by which its evolutionary pathway can be traced. In the case of stellar or 'dry' accretion, stars that have formed external to the main progenitor galaxy are accreted. The increase in mass is accompanied by a significant increase in galaxy radius, implying a reduction in mean density or 'puffing-up' of the galaxy (Bezanson

et al. 2009; Naab, Johansson & Ostriker 2009; van Dokkum et al. 2010; Hilz et al. 2012; Oogi & Habe 2013).

In contrast, the accretion of gas-rich satellite galaxies, or a 'wet' merger, may lead to only a minor increase in galaxy radius due to the dissipative nature of the gas (Barnes & Hernquist 1991; Mihos & Hernquist 1994). Depending on the detailed merger configuration (and gas richness), part of the gas may contribute to a relatively compact central starburst, increasing the mass density in the inner kpc (Sanders & Mirabel 1996), or more distributed star formation (Whitmore & Schweizer 1995; Renaud, Theis & Boily 2008).

Cosmological simulations indicate a two-phase evolution process for early-type galaxies (White & Rees 1978; Blumenthal et al. 1984; Oser et al. 2010). *In situ* star formation within the host galaxy dominates at high redshifts, followed by a period of mostly dissipationless mergers. Dry mergers promote inside-out growth, as stellar material accreted at large radii leaves the central regions of the galaxy unaffected (Hilz, Naab & Ostriker 2013; Bezanson et al. 2018; Karademir et al. 2019). In terms of the mass distribution of a galaxy, the two-phase model of late dry merger events would indicate that as redshift approaches zero, galaxies tend towards shallower total density gradients, with the density expressed by $\rho(r) \propto r^\gamma$.

★ E-mail: caro.derkenne@hdr.mq.edu.au

This two-phase evolution is supported by simulation studies that have traced the total mass density slopes through cosmic time. Total mass density slopes γ are found to be steeper at greater lookback times, and approximately constant below redshifts of $z \sim 1$, calculated over ~ 4 effective radii (R_e) (Remus et al. 2013, 2017; Xu et al. 2017; Springel et al. 2018; Wang et al. 2019; but see also Peirani et al. 2019). At redshifts of zero, the simulations indicate a convergence of density slopes around $\gamma \approx -2$, possibly as this 'isothermal' solution represents a low-energy, high-entropy state that galaxies evolve towards due to multiple stellar accretion events.

Observations of the total mass density slopes in the local Universe agree well with the predictions of simulations. Density slopes at low redshifts can be probed via multiple methods, such as tracing H I gas, the dynamics of planetary nebulae, and analysing the temperature of X-ray gas (Weijmans et al. 2008; Coccato et al. 2009; Humphrey & Buote 2010; Serra et al. 2016). The advent of integral field spectroscopy has provided access to detailed spatially resolved maps of stellar kinematics, allowing the application of more general dynamical modelling approaches that are better suited to the shapes and orbital anisotropies of real galaxies.

A small sample of local (<30 Mpc), fast-rotating early-type galaxies from the SLUGGS survey (Brodie et al. 2014) was used to derive total density slopes from Jeans modelling, finding $\overline{\gamma} = -2.19 \pm 0.03$ with a small intrinsic scatter of $\sigma_\gamma = 0.11$ (Cappellari et al. 2015). Poci, Cappellari & McDermid (2017) used a volume-limited sample of 258 early-type galaxies from the ATLAS^{3D} survey (Cappellari et al. 2011), reporting a mean of $\overline{\gamma} = -2.193 \pm 0.016$ for galaxies with a velocity dispersion above ~ 130 km s^{-1}, with an intrinsic scatter of $\sigma_\gamma = 0.168$. This sample extended to $\sim 1R_e$. ATLAS^{3D} was combined with SLUGGS data by Bellstedt et al. (2018), with an obtained density slope mean of $\overline{\gamma} = -2.12 \pm 0.05$, for an overlapping sample with Poci et al. (2017) but with a greater radial range ($\sim 4R_e$). A sample of 2778 early-type and spiral galaxies in the local Universe from the MaNGA survey (Bundy et al. 2014) found the highest mean density slope in the local Universe, with $\overline{\gamma} = -2.24$, with an intrinsic scatter of $\sigma_\gamma = 0.22$ (Li et al. 2019). However, this sample was not restricted to early-type galaxies. At a redshift of ~ 0, there is consensus on slightly steeper than isothermal density profiles.

At intermediate redshifts, density slopes are observationally probed by gravitational lensing, which provides a total integrated mass measurement within the Einstein radius based on how a more distant object's light is bent around the lens (Meylan et al. 2006). Studies of lensing systems in the Lenses Structures and Dynamics (LSD) survey (Koopmans & Treu 2004) found shallower ($\gamma \sim -1.75$) than isothermal mean slopes, from combining lensing mass measurements at large radii with mass measurements at small radii inferred from slit spectroscopy aperture velocity dispersions to model the total potential (Treu & Koopmans 2004; Koopmans et al. 2006). The slopes were for lensing systems across the redshift range $0.5 < z < 1$. A similar approach with a larger sample was conducted by Auger et al. (2010) using the Sloan Lens ACS Survey (SLACS), finding $\overline{\gamma} = -2.08 \pm 0.03$ for the redshift range $0 < z < 0.36$. Orbital isotropy was enforced in the models, which is not reflective of real galaxies (Cappellari et al. 2007).

Barnabè et al. (2011) combined gravitational lensing data with 2D stellar kinematic maps and two-integral Schwarzschild modelling to characterize a total mass potential, optimizing density profiles with a Bayesian inference approach. In these models, orbital anisotropy was also allowed. The obtained mean density slope from the 16 lens systems in this study is $\overline{\gamma} = -2.07 \pm 0.04$, for redshifts around $z \sim 0.2$, similar to Shajib et al. (2021). Subsequent studies using

combinations of data from SLACS, the LSD survey, the Strong Lenses in the Legacy Survey (Ruff et al. 2011), and the BOSS Emission-Line Lens Survey (Brownstein et al. 2011) found mild to significant trends with redshift, in that total density slopes were found to be systematically steeper at lower redshifts (Ruff et al. 2011; Bolton et al. 2012; Sonnenfeld et al. 2013). Contrary to the predictions of simulations, Bolton et al. (2012) found the most significant trend of shallow slopes at high redshifts to steeper slopes in the local Universe, of $d\langle\gamma\rangle/dz = 0.6 \pm 0.15$ for the redshift range $0 < z < 0.7$. Steepening slopes as redshift approaches zero are suggestive of the continued importance of dissipative processes in galaxy evolution (Sonnenfeld, Nipoti & Treu 2014) or potentially the occurrence of off-axis major mergers (Bolton et al. 2012).

The evolution with redshift implied by gravitational lensing results is at odds with the predictions of simulations, which indicate steeper slopes with higher redshifts (Remus et al. 2013, 2017; Wang et al. 2019), and is also inconsistent to the observed mass–size growth of early-type galaxies with redshift as inferred from stellar light (Franx et al. 2008; van Dokkum et al. 2010; van der Wel et al. 2014; Mowla et al. 2019). Furthermore, gravitational lensing is necessarily biased towards the most massive, dense objects that act as effective lenses, and this can impact knowledge of the distribution of total mass density slopes (Mandelbaum, van de Ven & Keeton 2009).

This work presents the results of Jeans anisotropic modelling on a sample of intermediate-redshift galaxies from the Frontier Fields clusters, in order to determine whether there exists a change in the distributions of density slopes at higher redshifts using identical methods to those of local Universe studies. Data from the Multi Unit Spectroscopic Explorer (MUSE) are used in combination with *Hubble Space Telescope* (*HST*) photometry to construct dynamical models by fitting 2D kinematic maps for 90 galaxies across the redshift range $0.29 < z < 0.55$. Section 2 describes the data sample obtained from the archives. Section 3 outlines the methods by which the kinematic fields and stellar potentials were determined, and the Jeans model definitions. Results are given in Section 4, and Section 5 places them in context with other studies. Conclusions are given in Section 6. Throughout, a standard, flat cosmology is adopted with *Wilkinson Microwave Anisotropy Probe 7* values of $H_0 = 70.2$ km s^{-1} Mpc^{-1}, $\Omega_\Lambda = 0.728$, and $\Omega_m = 0.272$ (Larson et al. 2011).

2 DATA SAMPLE

The six massive galaxy clusters comprising the Frontier Fields (Lotz et al. 2017) project represent a natural choice for building a sample of early-type galaxies at intermediate redshifts. Each cluster has overlapping *HST* and MUSE fields, and is rich in early-type galaxies suitable for deriving stellar kinematics and subsequent Jeans modelling. The early-type sample aims to be comparable with low-redshift samples such as ATLAS^{3D} (Cappellari et al. 2011) in terms of galaxy masses and sizes. Dense cluster environments have been shown to lead to truncation of the dark matter haloes of early-type galaxies in comparison to isolated field galaxies at the same redshift (Limousin et al. 2007; Eichner et al. 2013). However, this truncation occurs on scales outside the kinematic range of the data used to constrain the models used in this work, and is therefore not expected to strongly impact our results. We discuss the potential impact of environment further in Section 5.

The Frontier Fields project aims to observe massive galaxy clusters that act as lenses to even more distant objects, providing glimpses of the very early Universe. To that end, over 840 orbits of the *HST* were devoted to image the clusters in seven optical to near-infrared

Table 1. The ESO Science Archive ID for each of the data sets used in this work is provided, along with the MUSE programme IDs under which the data were originally obtained. The used PSF FWHM for the MUSE data is given, with further discussion in Section 3.3.

Cluster	ESO data ID	MUSE programme(s)	Effective exposure time (s)	PSF FWHM (arcsec)
A2744	ADP.2017-03-24T12:14:09.100	095.A-0181, 0.96.A-0496, 0.94.A-0115	16 345	0.64
AS1063	ADP.2017-03-28T12:46:01.331	095.A-0653	15 885	1.08
	ADP.2017-03-23T15:58:03.937	60.A-9345	7877	1.45
A370	ADP.2017-06-06T13:13:38.674	096.A-0710, 0.94.A-0115	13 655	0.72
M0416	ADP.2019-10-09T11:36:01.797	0.100.A-0763	39 545	0.740
	ADP.2017-03-24T16:19:17.624	0.94.A-0525	36 113	0.72
M1149	ADP.2017-03-24T16:26:09.634	294.A-5032	15 282	1.40

bands, being *F435W*, *F606W*, *F814W*, *F105W*, *F125W*, *F140W*, and *F160W*. In the *F814W* band used in this work, the target field exposure time is 105 ks, and the drizzled fields result in a spatial sampling of 0.03 arcsec per pixel.

All *HST* processed data were obtained from the STSci MAST Archive.[1] For this project, already reduced Epoch 1 or 2, version 1.0 drizzled science images were used. Details of the reduction process for the Frontier Fields *HST* images are given by Lotz et al. (2017), with a brief summary as follows. The data were reduced by masking sky artefacts and aligning to a standard astrometric grid, as well as calibrated with darks, flats, and bias fields. Where possible, fields were stacked to improve image depth.

The Frontier Fields clusters have overlapping, albeit smaller, MUSE/VLT fields. For the wide-field mode of MUSE used, the covered wavelength range is 480–930 nm, with a spatial scale of 0.2 arcsec per pixel over a 1 armin^2 field. The spectral resolution is ~50 kms^{-1} for ~6590 Å (Vaughan et al. 2018). The sky-region is split into 24 subfields via an advanced slicer, which then feed into 24 spectrographs; for details, see Bacon et al. (2010). Reduced science images from the MUSE-DEEP collection, in the form of 3D data and variance cubes, were obtained from the public ESO Archive Science Portal.[2] Briefly, the reduction involves bias removal, flat-fielding, astrometric calibration, flux calibration, and sky-subtraction. For details of the reduction pipeline, see Weilbacher et al. (2020). The data were taken without the aid of adaptive optics, with the point spread function (PSF) full width at half-maximum (FWHM) given in Table 1, along with integration times and data set IDs for the ESO Archive.

The Frontier Fields cluster M0717.5+3745 was not used in this work as it has no data in the optical band. The properties of the remaining five clusters – Abell 2744 (A2744), Abell S1063 (AS1063), Abell 370 (A370), MACS J0416.1−2403 (M0416), and MACS J1149.5+223 (M1149) – are summarized in Table 2, including the source used to determine cluster members.

3 METHODS

3.1 Stellar kinematics

The published world coordinates for each galaxy were used to extract individual galaxies from the main MUSE data cube. The size of each individual cube was constructed case-by-case by eye, creating the maximum isolated field possible, on average of extent $10R_e$, with the minimum case at $1.8R_e$. To ensure a reasonable signal-to-noise ratio (SNR) across the field, galaxies were thresholded to a median SNR of 2 per pixel in the wavelength range 5936–6997 Å for M1149 and

4998–7497 Å for the other clusters. All galaxies were Voronoi binned (Cappellari & Copin 2003) at an SNR of 10 per spectral pixel per bin for the given wavelength range. We conducted simulations (described in Appendix B) of the influence of the number of kinematics bins per field on the measured density slope, and concluded that at least five bins per field were necessary. Below this, the density slope could not be reliably constrained. A minimum threshold of at least five spatial bins per kinematic field is adopted here. On average the kinematics extend to about $3R_e$ for the targets in the present sample.

The Penalized PiXel-Fitting (PPXF) method (Cappellari & Emsellem 2004; Cappellari 2017) was chosen to recover the line-of-sight velocity distribution (LOSVD). The Medium resolution INT Library of Empirical Spectra (MILES[3]) single stellar population templates (version 11) (Vazdekis et al. 2010) were used to perform the fit, with a standard Salpeter initial mass function slope of 1.3 (Salpeter 1955), solar abundance iron content, with spectral FWHM resolution of 2.51 Å, and covering the wavelength range 3540–7410 Å. A central aperture spectrum and optimal template was first created for each galaxy to establish the required subset of templates, as done, for example, by van de Sande et al. (2017), reducing the freedom of the fit (and subsequent scatter in the kinematics) for the lower SNR bins. All spectra within $1R_e$ were co-added to create the central spectrum, using effective radii estimated by using the Source Extraction and Photometry library, the PYTHON implementation of Source Extractor (Bertin & Arnouts 1996; Barbary 2016). The central spectrum median SNR for the final sample, in the fitted wavelength range, is 26 within the $1R_e$ aperture, with a maximum in the sample of 120.

The central aperture spectrum was fitted, in rest-frame wavelengths, using PPXF with a second-order Legendre multiplicative polynomial and no additive polynomials. Additive polynomials change absorption line strengths, whilst multiplicative polynomials can correct for spectral calibration issues in the fit. The optimal template was created by the matrix multiplication of the weights of the fit with the input stellar library. No regularization was performed, as regularization smooths the weighting of each template's contribution to the optimal template to find star formation histories, which are not needed for dynamical models (Cappellari 2017). The first two moments of the stellar LOSVD were extracted by fitting all Voronoi-binned spectra with this optimal template, with iterative sigma-clipping to produce a 'clean' fit. A correction to the velocity dispersion value in each bin was performed after the fit, to account for the change in instrumental resolution of MUSE with wavelength. The correction was made by finding the difference between the broadening at each wavelength as measured for MUSE by Vaughan et al. (2018), and the broadening of the MILES library as measured

[1]doi:10.17909/T9KK5N
[2]http://archive.eso.org/scienceportal/home

[3]http://miles.iac.es/

Table 2. Data source to determine cluster members for each of the Frontier Fields galaxy clusters used in this work, shown in redshift order. The 'Members' column refers to galaxies within the archival MUSE footprint for each cluster, with the members drawn from the given source. The ID numbers used in this work correspond to the IDs in the given source, except for AS1063 and M1149, where the IDs correspond to those in Tortorelli et al. (2018). For A2744, the mass is a virial estimate within 1.3 Mpc (Merten et al. 2011); for AS1063, the given mass is an M500 estimate (Williamson et al. 2011); for A370, the given mass is a virial estimate (Richard et al. 2010); for M0416, the mass is a total mass within 950 kpc (Grillo et al. 2015); for M1149, the given mass is a total estimate (Zheng et al. 2012).

Cluster	Central coordinates (J2000)	Mass ($\times 10^{15}$ M$_\odot$)	Members	Cluster z	Source
A2744	00:14:21.2, −30:23:50.1	1.8	156	0.308	Mahler et al. (2018)
AS1063	22:48:44.4, −44:31:48.5	1.2	95	0.348	Karman et al. (2015)
A370	02:39:52.9, −01:34:36.5	∼1	56	0.375	Lagattuta et al. (2017)
M0416	04:16:08.9, −24:04:28.7	1.4	193	0.396	Caminha et al. (2017)
M1149	11:49:36.3, +22:23:58.1	2.5	68	0.542	Grillo et al. (2016)

by Falcón-Barroso et al. (2011). This correction term was added in quadrature to the velocity dispersion in each bin. Uncertainties for the derived values in each bin were estimated via a Monte Carlo process using 100 trials and shuffling the residuals of the fit for each iteration. All kinematic fields can be seen in Fig. A1. Examples of the obtained kinematic fields, central spectra, and *HST* images can be seen in Fig. 1.

3.2 Photometry

The photometry analysis presented here is based from *HST* data in the *F814W* band. Inferring the intrinsic luminosity distribution within a galaxy from its projected surface brightness involves parametrizing the observed light distribution in such a way as to allow different assumed viewing angles to be tested. The multi-Gaussian expansion (MGE) method describes the galaxy surface brightness via a combination of positive, concentric, 2D Gaussians (Monnet, Bacon & Emsellem 1992; Emsellem, Monnet & Bacon 1994). Here, we use the PYTHON package MGEFIT (Cappellari 2002).[4] The surface density is described, as in equation (1) in Cappellari (2002), as

$$\Sigma(x', y') = \sum_{j=1}^{N} \frac{L_j}{2\pi \sigma_j^2 q_j'} \exp\left[-\frac{1}{2\sigma_j^2} \left(x_j'^2 + \frac{y_j'^2}{q_j'^2} \right) \right], \qquad (1)$$

where (x', y') are observed (projected) coordinates centred on the galaxy and are aligned with the photometric major axis, N is the number of included Gaussian components, each of luminosity L_j; q_j' is axial ratio of the Gaussian component, or flattening; σ_j is the dispersion of the Gaussian component measured along the major axis of the galaxy. This parametrization is conducted in image units – pixels and counts. In this formalism, the position angle (ψ) is measured counter-clockwise from the image y-axis (North oriented for this project). The galaxy centre in image coordinates and position angle are both determined by the MGEFIT routine. The polar coordinates R' and θ' are related to the sky coordinates via

$$x_j' = R' \sin(\theta' - \psi_j) \qquad (2)$$

$$y_j' = R' \cos(\theta' - \psi_j). \qquad (3)$$

In the axisymmetric case, where a galaxy is assumed to be an oblate spheroid, the flattest Gaussian in the MGE model sets the minimum allowed inclination (corresponding to an infinitely thin disc). The roundest Gaussians consistent with the photometric data was fit in order to avoid overconstraining the Jeans dynamical models, as done

by Scott et al. (2013). The relation between the Gaussian flattening and inclination is given by

$$q_j^2 = \frac{q_j'^2 - \cos^2 i}{\sin^2 i}, \qquad (4)$$

where q is the intrinsic axial ratio and q' is the projected axial ratio on the plane of the sky, with i being the inclination. The deprojected axisymmetric oblate luminosity density is then given by

$$\nu(R, z) = \sum_{j=1}^{N} \frac{L_j}{(\sqrt{2\pi}\sigma_j)^3 q_j} \exp\left[-\frac{1}{2\sigma_j^2} \left(R^2 + \frac{z^2}{q_j^2} \right) \right], \qquad (5)$$

following equation (13) of Cappellari (2008). To construct each MGE, individual galaxies were isolated from the main *HST* field, with masking of adjacent sources performed as necessary. At this step, any galaxy with an irregular or spiral morphology was rejected from the sample. Using the MGEFIT package, the central pixel coordinates, major and minor axes, position angle, and ellipticity were fitted. The galaxy image was divided into sectors spaced linearly in angle and logarithmically in radius; at each sector, the radius, angle, and intensity in counts were recorded. The success of the process was visually judged by overplotting the fit on the galaxy isophotes in regular magnitude steps, and visually inspecting the corresponding 1D sector fits. The central region of each MGE fit can be seen in Fig. A1. The effective radius was derived as the circularized arcsecond extent that contains half the measured luminosity of each MGE, using the total counts from the MGE and the radii in pixel units. This was converted to physical units (kpc) using a distance estimate to each galaxy based on the mean cluster redshift and the assumed cosmology. This is the effective radius (R_e) reported for each galaxy in Table A1 and used in all subsequent analysis. The luminous MGE surface density can remain in arbitrary units as a total potential model set-up is used, described in Section 3.3. The luminous MGE dispersion is converted to physical units by multiplying by the *HST* pixel scale of 0.03 arcsec per pixel.
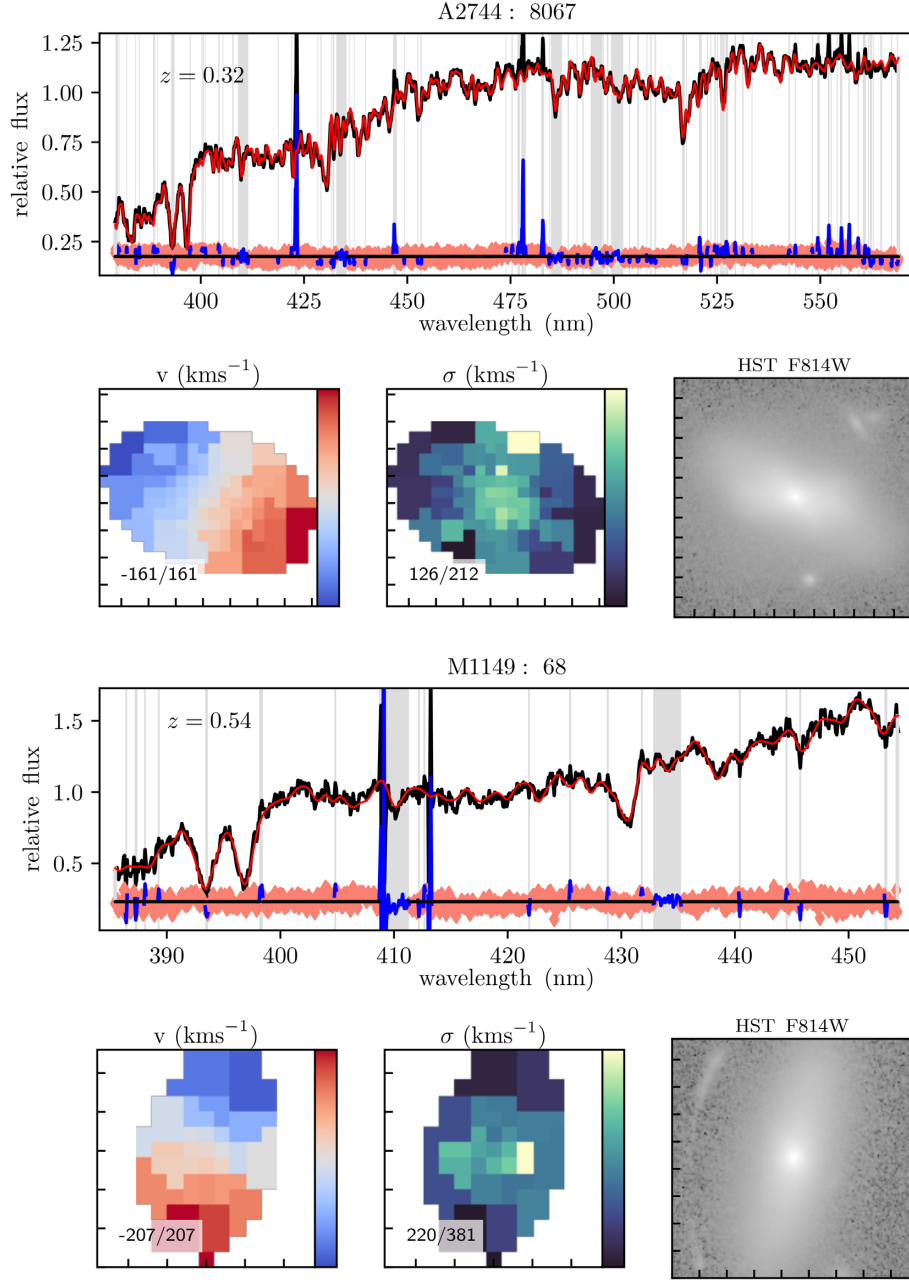
3.3 Jeans modelling

This project utilizes Jeans anisotropic modelling (JAM) through the JAMPY package (Cappellari 2008).[5] One of the important inclusions of using the JAM technique is accounting for deviation from perfectly isotropic orbital structures, through the anisotropy parameter, β_z,

---

[4]https://pypi.org/project/mgefit/

[5]https://pypi.org/project/jampy/

Figure 1. An example of the fields from a low-redshift (A2744 8067, $z \sim 0.32$) and a comparatively high-redshift (M1149 68, $z \sim 0.54$) galaxy. The rest-frame $1R_e$ aperture spectrum is shown (black) with the PPXF fit overplotted (red). Residuals (pink) are at the bottom of the panel, with excluded sections of spectrum shown (blue and grey). The velocity and velocity dispersion fields are shown, with the inset numbers indicating the scale of the colours in km s^{-1}. The *HST F814W*-band thumbnail of the galaxy is shown. All tick marks correspond to 0.5 arcsec.

defined as

$$\beta_z \equiv 1 - \left(\frac{\sigma_z}{\sigma_R}\right)^2 \qquad (6)$$

where R denotes the radial direction and z is along the axis of symmetry. JAMPY models the observed kinematics, predicting the second moment of the velocity distribution for the luminous barycentres of each projected position – in this case, the Voronoi bin centroids – of the galaxy, integrated along the line of sight. These predictions are derived by deprojecting the MGE model into an intrinsic gravitational potential for a given inclination. The quality of the fit is judged by a chi-square statistic, which takes each data bin as a degree of freedom. Following Cappellari (2008), the JAM

formalism makes two key simplifying assumptions: (1) the velocity ellipsoid is aligned with the cylindrical coordinate system (R, z, ϕ); and (2) the anisotropy is spatially constant, for this implementation of the models. The relationship between the gravitational potential (Φ), luminosity density (ν, defined in equation 5), and moments of velocity (v) is then derived from the Jeans equations in the general case as

$$\frac{\frac{1}{1-\beta_z}\nu\overline{v_z^2} - \nu\overline{v_\phi^2}}{R} + \frac{\partial\left(\frac{1}{1-\beta_z}\nu\overline{v_z^2}\right)}{\partial R} = -\nu\frac{\partial\Phi}{\partial R}, \qquad (7)$$

$$\frac{\partial(\nu\overline{v_z^2})}{\partial z} = -\nu\frac{\partial\Phi}{\partial z}, \qquad (8)$$

following equations (8) and (9) in Cappellari (2008). The shorthand notation

$$\nu \overline{v_k v_j} \equiv \int v_k v_j f \, d^3 \boldsymbol{v} \tag{9}$$

has been used, with f the distribution function of the stars and the total gravitational potential set in this case by an MGE model, and as defined in Emsellem et al. (1994) equations (39) and (40). The observed kinematics for each field were combined into a single $v_{\rm rms}$ field, defined as $v_{\rm rms} = \sqrt{v^2 + \sigma^2}$. For each individual Voronoi bin there exists a single $v_{\rm rms}$ value, the sky-plane spatial location of which is set by the luminous barycentre of the bin. Weighting was given to each bin by use of an error vector, defined as

$$\delta v_{\rm rms} = \frac{\sqrt{(v \times \delta v)^2 + (\sigma \times \delta \sigma)^2}}{v_{\rm rms}}, \tag{10}$$

where the uncertainty on v and σ are those obtained from the kinematics Monte Carlo process. The coordinates for each bin were rotated by the galaxy position angle, so that the x-axis aligns with the galaxy projected major axis. Further, the velocity and dispersion fields were bi-symmetrized prior to their combination into a single $v_{\rm rms}$ field. The symmetrization reduces outliers that form solutions away from the axisymmetric case, by mapping $x_j \rightarrow (x_j, -x_j, x_j, -x_j)$, and similarly for y_j.

The kinematics of each model are convolved with the PSF of the data in order to derive a goodness of fit. A normalized circular MGE model is used to describe the MUSE point spread function (PSF). This was either estimated by fitting stars in the MUSE field, or using the seeing FWHM estimated in the archival data fits header. Both were found to agree within 5 per cent of each other in cases where stars were available in the field. The effects of the PSF estimation on the density slopes were explored and found to be minimal, for details see Appendix B.

The gravitational effect of a central supermassive black hole is well below the spatial resolution of the kinematic data. For completeness, however, a central unresolved dark mass component of mass

$$\log_{10} M_{\rm bh} = 8.01 + 3.87 \log_{10}(\sigma_e/200 \, \text{km s}^{-1})$$
$$- 0.138 \log_{10}(1 + z) \tag{11}$$

was included in each model, as given in equation (5) of Robertson et al. (2006).

A total generalized potential was implemented for each model, which is representative of early-type galaxy mass distributions, where baryonic matter sits within an extended dark matter halo (White & Rees 1978; Blumenthal et al. 1984). The general potential used in this work is a double-spherical power law of the form

$$\rho(r) = \rho_s \left(\frac{r}{r_s}\right)^{\gamma'} \left(\frac{1}{2} + \frac{1}{2}\frac{r}{r_s}\right)^{-\gamma'-3}, \tag{12}$$

where γ' and -3 represent the inner and outer total-mass density slopes, separated by the break radius r_s, and normalized to ρ_s, the density at r_s. This is a general form of a so-called Nuker Law (Lauer et al. 1995), assuming a Navarro–Frenk–White dark matter halo (Navarro, Frenk & White 1997). For this project, as done by Poci et al. (2017), the break radius r_s was set at 20 kpc, with the maximum radius, $r_{\rm m}$, set as 25 kpc. This definition ensures that the outer regions can be fixed to a cosmologically motivated slope without influencing the central regions, which are then free to vary in response to the kinematic data. Arcsecond and parsec scales were converted using the cosmology calculator of Wright (2006).

A Monte Carlo Markov chain approach was used for the parameter estimation, via the PYTHON package EMCEE (Foreman-Mackey et al.

2013; Hogg & Foreman-Mackey 2018).[6] The models as implemented here have four free parameters: the inner density slope γ', the density at the break radius ρ_s, the orbital anisotropy β_z, and the inclination of the galaxy, i. Flat priors were set, with $-4 < \log_{10}(\rho_s) < 0$, $-3.5 < \gamma' < -0.5$, $-0.5 < \beta < 0.5$ and inclination between the minimum angle set by the MGE and $90°$. These ranges were chosen to be broadly consistent with dynamical modelling conducted at redshift zero (Poci et al. 2017; Bellstedt et al. 2018).

A maximum of 10 000 steps was set with 50 independent walkers. A run could terminate earlier if the chain was longer than 50 times the estimated autocorrelation time, providing the autocorrelation time estimates were stable. The median of the chain for each parameter was used to estimate the most likely parameter value, with the 1σ uncertainty given by the 16th and 84th percentiles, respectively. The best-fitting model is defined as the model built from the median values of each parameter chain. Each chain had the initial steps corresponding to twice the galaxy autocorrelation time estimate, or 'burn-in', removed. If the median density slope estimate was not more than 2σ removed from either boundary, the galaxy was rejected from further analysis, taking the final sample to 90 galaxies across the five clusters. The removal of these poorly constrained cases has not affected the conclusions of this work. A corner plot of the parameter distributions and the resulting median-fit JAM model for two galaxies are shown in Fig. 2.

As done by Poci et al. (2017), the average logarithmic slope of the total mass density profile is defined as

$$\gamma = \frac{\log_{10}(\rho(R_o)/\rho(R_i))}{\log_{10}(R_o/R_i)}, \tag{13}$$

with R_o set as the maximum extent of the kinematic data and R_i set as the radius of the MUSE PSF for each cluster. As also found by Bellstedt et al. (2018), the average slope γ is slightly steeper than the EMCEE optimized slope γ'. This difference is due to the kinematic data extending on average to $3R_e$, where the transition between the inner slope γ' and post-break radius slope (set as -3) becomes important.

4 RESULTS

The density slopes for the 90 galaxies in the Frontier Fields sample are found using equation (13). All derived density slopes, aperture dispersions, effective radii, and dynamical masses can be found in Table A1. All visual outputs (kinematic fields, modelled fields, and MGEs) can be seen in Fig. A1.

In general, the anisotropy and inclination of each galaxy were unconstrained in the EMCEE posterior distributions. Both parameters were included to accurately reflect the uncertainty on the density slope and avoid driving the density slopes to solutions motivated by inaccurate anisotropy or inclination values. The priors were set such they span a realistic range of anisotropies as observed in local Universe studies (Cappellari et al. 2013).

For some galaxies with a low number of spatial elements across the field (for example, galaxy 4439 in cluster A2744, in Fig. A1), the derived density slopes were well constrained in terms of uncertainties at the level of ~15 per cent. This constraint is at face value surprising, as with few spatial elements, structure such as clear rotation or comparatively high central dispersion is unobservable. However, as a global potential is set, only a small parameter space of break-radius densities and inner density slopes lead to an integrated mass that

[6] https://emcee.readthedocs.io/en/stable/
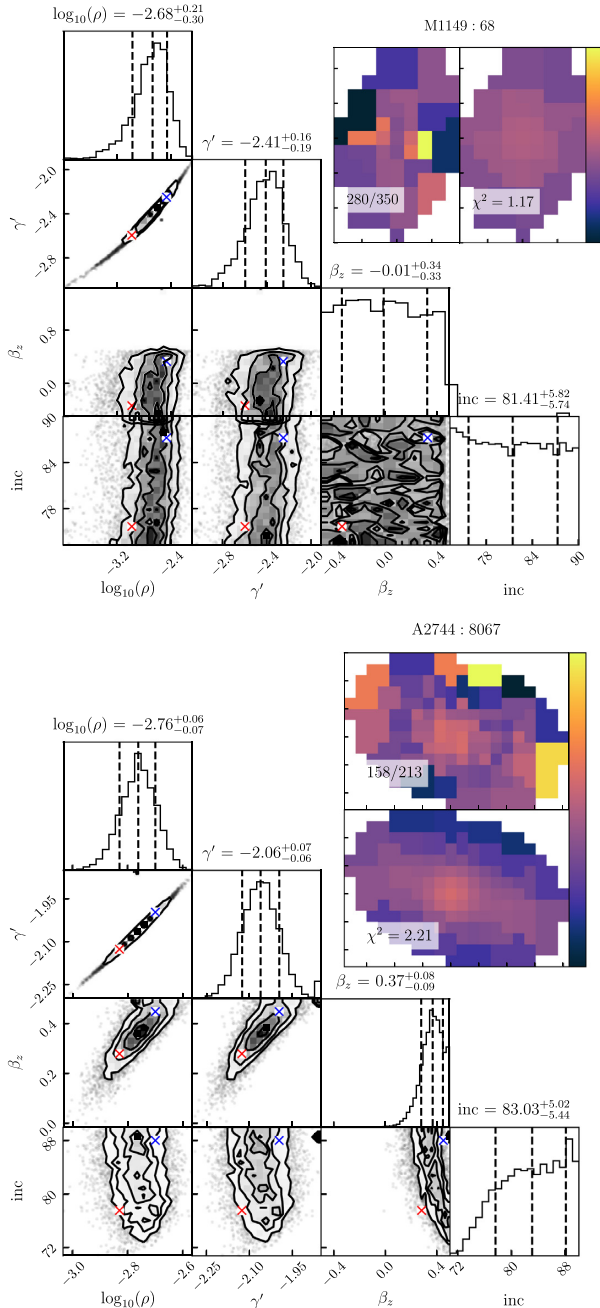
Figure 2. The sampling of the parameter space by the walkers is shown with the marginalized histograms on the top. The observed v_{rms} field and the modelled field are also shown, for galaxies M1149:68 and A2744:8067 as in Fig. 1. The colour scale is marked on the observed field in units of km s^{-1}, and the reduced chi-square value shown on the modelled field. For the two fields, ticks indicate 0.5 arcsec. The red and blue crosses are relevant for Fig. A1. The red crosses show the parameter values used to construct the 16th percentile v_{rms} fields (in column 5), and the blue crosses show the parameters used to construct the 84th percentile v_{rms} fields (in column 7).

Figure 3. The Frontier Fields sample total density profiles are shown in the top panel, with isothermal and sub- and superisothermal slopes shown for reference. The profiles are plotted between the kinematic MUSE psf radius for each cluster to the maximum kinematic data extent. These profiles are obtained from the models. The total profiles have density slopes around isothermal values. Stellar profiles measured directly from the stellar MGEs are shown on the bottom panel, between the radial range 0.16 arcsec to the maximum kinematics extent. The inner radius is chosen in both cases to avoid PSF effects of MUSE and the *HST*, respectively. The stellar profiles are on average steeper than isothermal.

steep or shallow lead to a mean v_{rms} value that is too high or low, respectively.
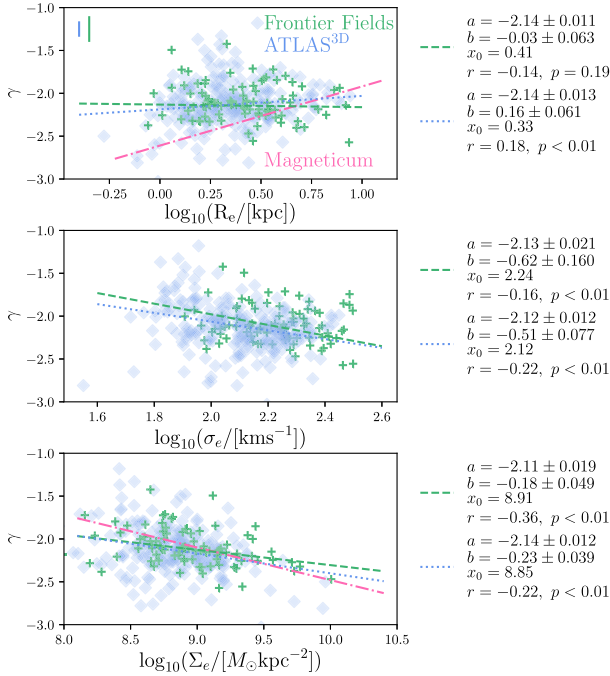
The derived total density profiles and the accompanying stellar density profiles are shown in Fig. 3. The stellar profiles were computed directly from the stellar MGES fitted to the *HST* data, across the radial range of 0.16 arcsec to the maximum kinematic extent of the data. The inner radius is set so as to conservatively avoid the *HST* PSF. The total density slopes have a median of $\gamma = -2.11 \pm 0.03$. The distribution has a standard deviation of 0.21 and a median 1σ uncertainty on each slope of 0.11. The stellar slopes are on average steeper than the total slopes, with a median of $\gamma_\star = -2.86 \pm 0.05$, and a standard deviation of 0.32.

4.1 Correlations with total mass density slope

The LtsFit[7] procedure of Cappellari et al. (2013) was used to investigate correlations between the total density slope and structural properties in the Frontier Fields sample. All fits and underlying data can be seen in Fig. 4.

For the Frontier Fields sample, no significant correlation with (log) effective radius was found, consistent with the trend observed in the ATLAS^{3D} sample within 1σ. Comparing to trends from simulations, we see that the Magneticum simulation early-type galaxies show a significant correlation with effective radius, where

can replicate the observed kinematics. Even with few constraints, the dynamical mass found by JAMPY is robust, as the mass directly impacts the observed kinematics, with no intermediate assumptions concerning the relative distributions of baryons and dark matter. As can be seen in Fig. A1 columns 5 and 7, density slopes that are too

---

[7]https://pypi.org/project/ltsfit/

Figure 4. The observed relationships between density slope and effective radius (top panel), velocity dispersion (middle panel), and surface mass density (bottom panel) for the Frontier Fields sample (green) and ATLAS[3D] sample (blue). The green and blue dashed lines show the best fit obtained by the LtsFit procedure for the Frontier Fields and ATLAS[3D] samples, respectively, in the form $y = a + b(x - x_0)$. The best-fitting parameters, corresponding errors, and Pearson coefficients with p-values are inset. A representative error on the density slope for each sample is shown in the top left corner of the top panel. The ATLAS[3D] sample effective radii are from Cappellari et al. (2011), with the velocity dispersions from Cappellari et al. (2013), and slopes from Poci et al. (2017). The LtsFit procedure was applied to the ATLAS[3D] sample in the same way as for the Frontier Fields galaxies. The Magneticum relation between density slope and effective radius is shown in the top panel, of form $\gamma = 0.69\log(R_e - 2.61)$. The Magneticum relation between density slope and surface mass density is shown on the bottom panel, of form $\gamma = -0.38\log(\Sigma_\star) + 1.32$. The Magneticum fits are from Remus et al. (2017).

galaxies with a smaller effective radius have on average steeper density slopes, with the linear fits remaining constant across different redshift ranges (Remus et al. 2017). The gradient of the Magneticum relation, $d\gamma/dR_e = 0.69$, is very similar to the redshift zero trend of the IllustrisTNG early-type galaxies of $d\gamma/dR_e = 0.64$. Using the SL2S, SLACS, and LSD samples, Sonnenfeld et al. (2013) report a comparable trend of density slope with effective radius of $d\gamma/dR_e = 0.76 \pm 0.15$ for fixed redshift and mass, steeper than the SLACS only trend of $d\gamma/dR_e = 0.41 \pm 0.12$ found by Auger et al. (2010) for $0 < z < 0.36$. In summary, the observed trends between density slope and effective radius in the ATLAS[3D] and Frontier Fields samples are therefore not in agreement with the comparatively steep Magneticum, IllustrisTNG, and lensing relations.

A trend between density slope and velocity dispersion is observed, seen in the middle panel of Fig. 4. The Frontier Fields sample has a marginally steeper relation with velocity dispersion ($d\gamma/d\sigma_e = -0.62$) than the ATLAS[3D] sample ($d\gamma/d\sigma_e = -0.51$), with high dispersion galaxies having steeper observed density slopes. However, given the scatter in the data, the recovered trends between samples are consistent within the measurement errors. No pronounced trend between central velocity dispersion and total density slope is found

in the IllustrisTNG simulations for redshift zero (Wang et al. 2020), contrary to the relatively steep relation found here.

A near identical trend between the Frontier Fields and ATLAS[3D] samples was calculated for the relationship between total surface mass density and the total mass density slope, seen in the bottom panel of Fig. 4. The Magneticum relation is also shown for the stellar mass surface density, which Remus et al. (2017) found to be redshift independent. The surface density is defined as

$$\Sigma_e = \frac{0.5 \times M}{\pi R_e^2},\tag{14}$$

where the total mass, M, is twice the mass computed by integrating the best-fitting total potential within a sphere of radius one R_e, as in Cappellari et al. (2013). The total masses used for this calculation are given in Table A1. Across both samples, objects with high surface mass densities have steeper slopes, indicating compact objects have correspondingly steep density profiles, as naively expected, with a gradient of $d\gamma/d\Sigma_e = -0.18$ for the Frontier Fields sample, and a gradient of $d\gamma/d\Sigma_e = -0.23$ for the ATLAS[3D] sample. Sonnenfeld et al. (2013) report a trend of $\delta\gamma/\delta\log\Sigma_\star = -0.38 \pm 0.07$ for gravitational lensing results, identical to the Magneticum relation for early-type galaxies (Remus et al. 2017), both using a stellar surface mass density instead of a total surface mass density. The steepest relation is given for the IllustrisTNG early-type galaxies, of $d\gamma/d\Sigma_\star = -0.45 \pm 0.02$ at $z = 0$ (Wang et al. 2020).

The agreement of the above trends in the ATLAS[3D] and Frontier Fields samples, despite the different redshifts, indicates the dependence of the density slope on these structural parameters is independent of redshift. This is in agreement with the results from Remus et al. (2017), who also found the correlations with stellar surface mass density and effective radius to be independent of redshift for the Magneticum early-type galaxy sample.

All density slope values for the Frontier Fields sample are shown against redshift in Fig. 5. No significant correlation is observed between density slopes in the Frontier Fields sample and redshift in the range $0.29 < z < 0.55$. However, strong evidence for evolution in the small redshift range of the Frontier Fields sample is not expected, considering also the intrinsic scatter of the sample and associated density slope uncertainties. The IllustrisTNG simulations indicate little evolution in density slope below $z \sim 1$, due to evolution via gas-poor mergers (Wang et al. 2019). The Magneticum simulations predict a mild trend with redshift given by the relation $\langle\gamma\rangle = -0.21z - 2.03$ (Remus et al. 2017). Gravitational lensing indicates density slopes were shallow at high redshifts, and have progressively become steeper as redshift approaches zero, with the most pronounced relation being $d\langle\gamma\rangle/dz = 0.60 \pm 0.15$ (Bolton et al. 2012) for the redshift range $0.1 < z < 0.7$. Using the SL2S, SLACS, and LSD samples, Ruff et al. (2011) finds a milder redshift trend of $d\langle\gamma\rangle/dz = 0.25^{+0.10}_{-0.12}$, up to redshifts of $z \sim 1$. A similar analysis presented by Sonnenfeld et al. (2013) with 25 lensing systems from SL2S found a redshift trend $d\langle\gamma\rangle/dz = 0.31 \pm 0.10$, for $0.2 < z < 0.8$. There is no evidence of shallower slopes at greater lookback times in the Frontier Fields sample, contrary to the results of gravitational lensing.

4.2 Comparison to simulations at $0.29 < z < 0.55$

The distribution of total mass density slopes of the Frontier Fields sample was compared to the distribution of total mass density slopes calculated from early-type galaxies in the Magneticum simulations (Teklu et al. 2015; Remus et al. 2017) and early-type galaxies in the IllustrisTNG100 simulations (Pillepich et al. 2018; Springel
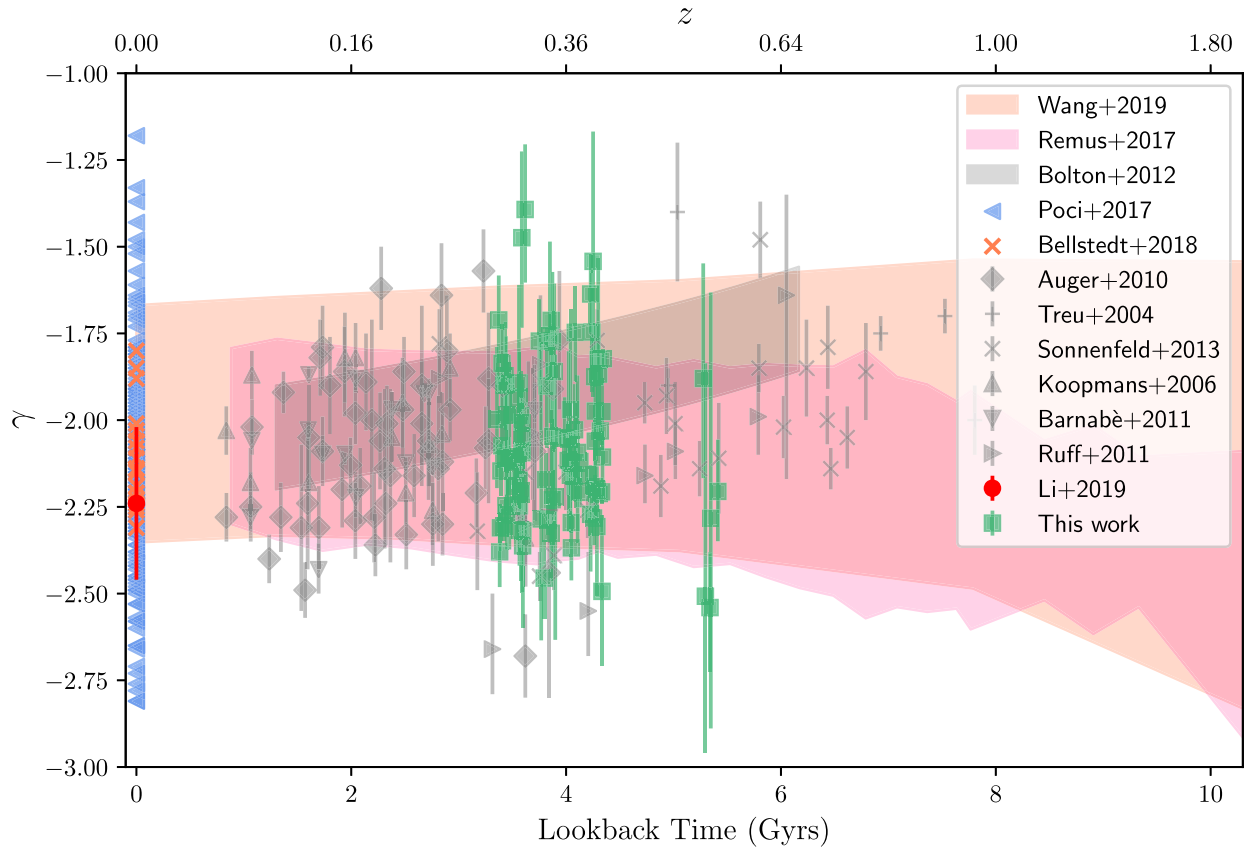
Figure 5. Measured density slopes using different methods are shown. At redshift zero, for context, are the results of Poci et al. (2017) Model I, which is an identical model construction to the generalized potential used in this work. The IllustrisTNG results, from Wang et al. (2019) are across seven redshifts bins (0, 0.1, 0.2, 0.3, 0.5, 1, 2), and the results are shown as an orange region, of width equal to the twice standard deviation at each redshift. Magneticum simulation results are shown as a pink shaded region, defined here by a parabolic fit to the model predictions, with width equal to twice the standard deviation of the density slopes at each redshift. All gravitational lensing results are shown in grey: see Treu & Koopmans (2004), Koopmans et al. (2006), Auger et al. (2010), Ruff et al. (2011), Barnabè et al. (2011), and Sonnenfeld et al. (2013). The density slope evolution with redshift measured by (Bolton et al. 2012) is shown as a black shaded band, with width corresponding to the quoted uncertainty. The derived density slopes for this work are shown in green with their 1σ uncertainty, corresponding to the 16th and 84th percentiles of the EMCEE distribution.

et al. 2018), shown in Fig. 6. The cumulative distribution of the samples is shown in the bottom panel. To make this comparison, only Magneticum early-type galaxies (724 galaxies) in the redshift range $0.29 < z < 0.55$ were used, and early-type IllustrisTNG galaxies in two redshift bins ($z = 0.3$ and $z = 0.5$, 1432 galaxies).

The total mass density slopes of the Frontier Fields sample at this redshift agree well with the predictions of the Magneticum simulations in terms of their medians. A Kolmogorov–Smirnov (KS) two-sample test performed on the Magneticum and Frontier Fields density slopes yields a KS test statistic of 0.13, and a critical value of 0.18 for $\alpha = 0.01$. The obtained p-value is 0.10, failing to reject the null hypothesis the samples share a common distribution. The Magneticum simulation prediction of density slopes for early-type galaxies are therefore consistent with the observed Frontier Fields galaxy slopes in the same redshift range.

The IllustrisTNG sample has on average shallower slopes for the same redshift, with a skew distribution towards steeper slopes, indicating a predominance of more compact objects in that sample. The IllustrisTNG early-type galaxy density slopes are not consistent with the Frontier Fields sample slopes, with the medians differing by more than 3σ. A KS test for the two samples gives a test statistic of 0.35, a critical value of 0.1769, and a p-value of 7×10^{-10}, indicating the IllustrisTNG and Frontier Fields sample do not share

a common distribution. The shallower IllustrisTNG slopes may arise due to the level of included active galactic nucleus (AGN) feedback in the models, which quenches *in situ* star formation, removes baryonic matter from central regions, and causes density slopes to approach isothermal values (Wang et al. 2019, 2020). In particular, Wang et al. (2019) find AGN feedback energy through the kinetic mode (the ejection of kinetic energy and momentum into surrounding gas cells without thermal energy) as implemented in the IllustrisTNG simulations dominates the change of density slopes towards shallower values in the redshift range $1 < z < 2$, after which the density slope is near invariant.

4.3 Comparison to local Universe density slopes

The derived total mass density slopes in comparison to other studies, as a function of redshift, are shown in Fig. 5. A unique aspect of this work is that we apply exactly the exact same methodology to the Frontier Fields sample as applied to the local ATLAS^{3D} sample, allowing the two sets of density slope values to be directly compared. In particular, the comparison was made using the 'Model I' results of Poci et al. (2017), where the same generalized potential is used, in the form of a spherical double power law. A point of difference between the samples is the radial range, which extends to $3R_e$ on average
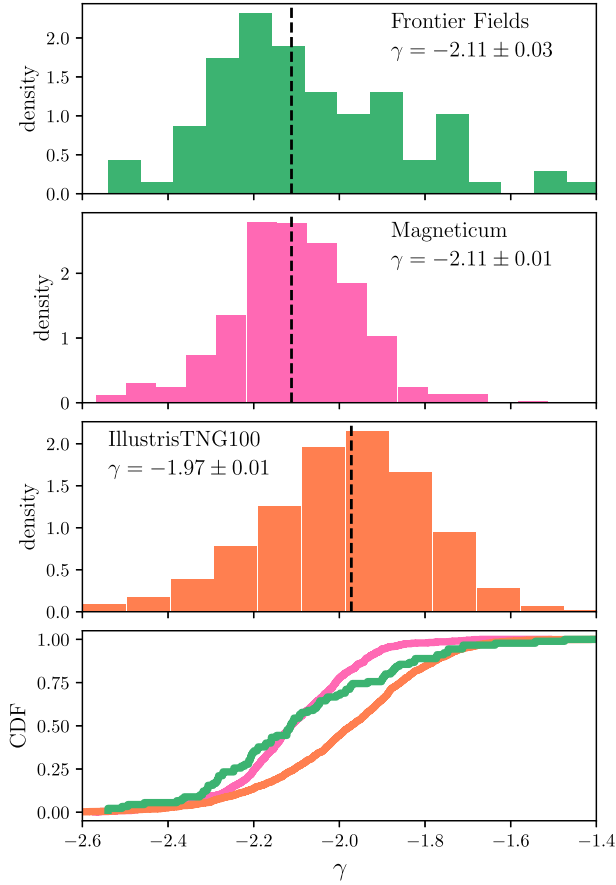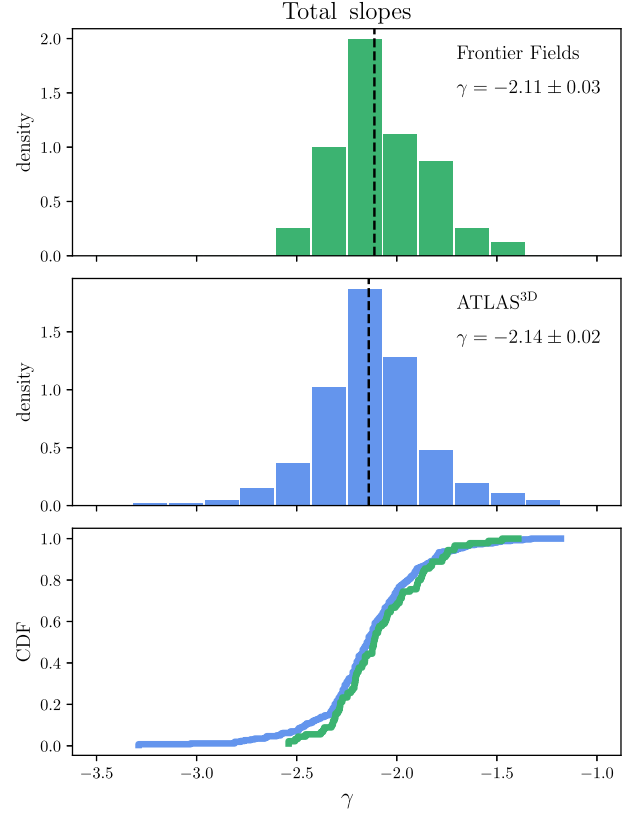
Figure 6. The Frontier Fields sample density slopes (green) compared to the Magneticum simulation galaxy density slopes (pink) and IllustrisTNG density slopes (orange). The histograms are plotted as density distributions instead of frequency. Inset are the median density slope and associated standard error. The bottom panel shows the cumulative distribution function (CDF) of each sample, which forms the basis of the KS tests.

for the Frontier Fields galaxies, and $1R_e$ for the ATLAS^{3D} sample. However, Bellstedt et al. (2018) find a comparable mean density slope using a subset of the ATLAS^{3D} sample with the dynamical models constrained up to $4R_e$, signifying the differences in radial range between the ATLAS^{3D} sample and Frontier Fields sample is not problematic. Furthermore, Cappellari et al. (2015) find a power law with constant logarithmic slope γ is an accurate description of the total mass density slope across the radial range $0.1-4R_e$.

The distribution of density slopes for the 258 galaxies of the ATLAS^{3D} sample is compared to the Frontier Fields sample in Fig. 7. The ATLAS^{3D} sample has a median value and standard error of $\gamma = -2.14 \pm 0.02$, and the Frontier Fields sample of $\gamma = -2.11 \pm 0.03$. This result is in good agreement with the results of Bellstedt et al. (2018), who found $\langle \gamma \rangle = -2.12 \pm 0.05$ for 21 early-type galaxies, but is shallower than the ManGA mean density slope of $\langle \gamma \rangle = -2.24$ (Li et al. 2019). However, the ManGA sample is not restricted to early-type galaxies.

The ATLAS^{3D} sample has a tail of steeper density slopes that are not observed in the Frontier Fields sample, seen in Fig. 7. Given the correlations discussed in Section 4.1, this tail represents compact galaxies with high surface mass densities. A tail of shallow density slopes is also missing from the Frontier Fields sample, which could be an effect of extended, low surface brightness galaxies being difficult to observe at large distances. It is possible the dense


Figure 7. The top panel (green) shows the density histogram of the Frontier Fields sample with the median density slope and standard error inset. The lower panel (blue) shows the density histogram of the ATLAS^{3D} sample of Poci et al. (2017) at redshift zero, with the median slope and standard error inset. The cumulative distribution of the two samples is shown on the bottom panel.

cluster environment of the Frontier Fields sample also had an effect. However, no statistical difference was found between the subsample of ATLAS^{3D} drawn from the Virgo cluster and the ATLAS^{3D} sample as a whole, suggesting environmental differences do not significantly impact density slope distributions. Note the comparison of total mass density slopes is drawn against the full ATLAS^{3D} sample of galaxies. A break has been reported in the $\gamma - \sigma_e$ relation, where the density slope depends on the velocity dispersion of galaxies with a central dispersion below ~ 100 kms^{-1}. Density slopes are found to be independent of velocity dispersion for values above ~ 100 kms^{-1} (Poci et al. 2017; Li et al. 2019). The agreement between the Frontier Fields sample and the ATLAS^{3D} sample is not impacted by only considering galaxies for which $\sigma_e > 100$ kms^{-1}.

A KS test was performed between the ATLAS^{3D} and Frontier Fields samples, with the CDF shown in the bottom panel of Fig. 7. A KS test statistic of 0.10 was obtained for a critical value of 0.19, with $\alpha = 0.01$, and a p-value of 0.47. The null hypothesis that the samples share a common distribution is not rejected. As the same methods were used to derive the density slopes for the ATLAS^{3D} and Frontier Fields sample, the indication of the KS statistic that the samples were drawn from comparable distributions reveals no evolution of the total density slope in the last ~ 6 Gyr of cosmic time.

From the MGE fits to the *HST* photometry, stellar density slopes are also derived for the Frontier Fields, defined here as

$$\gamma_\star = \frac{\log_{10}\left(\rho_\star(R_o)/\rho_\star(R_i)\right)}{\log_{10}\left(R_o/R_i\right)}, \tag{15}$$
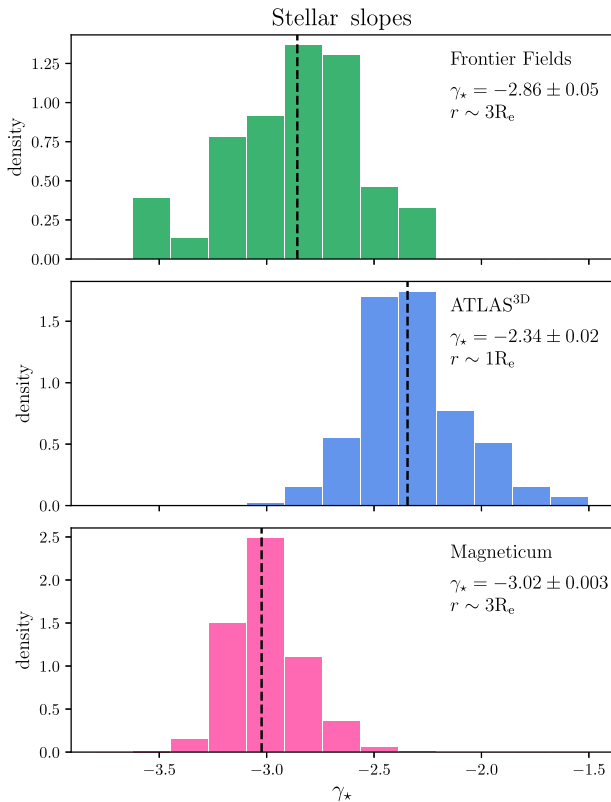
Figure 8. The Frontier Fields sample stellar density slopes (green) as measured from the stellar MGEs, compared to the stellar density slopes of the ATLAS[3D] sample (blue), measured from the MGEs of Scott et al. (2013). The median value and its associated standard error is shown for each sample. The ATLAS[3D] stellar slopes are calculated up to $1R_e$, while the Frontier Fields sample is calculated to $3R_e$ on average. The Magneticum slopes shown on the bottom panel (pink) are calculated up to $3R_e$, and are shown for the redshift range of the Frontier Fields sample. The difference in radial ranges prevents a robust comparison between the distributions.

with $\rho_\star$ the stellar density inferred from the MGEs, and R_i and R_o the inner and outer radius, respectively. The same method is applied to the ATLAS[3D] galaxies using the MGEs of Scott et al. (2013). However, due to the differences in PSF sizes and the spatial coverage of the MGEs, the Frontier Fields stellar slopes are computed across the radial range 0.16 arcsec to the maximum kinematic extent of the data (on average $3R_e$), while the ATLAS[3D] stellar slopes are computed across the radial range 2 arcsec to the maximum kinematic extent (on average $1R_e$).

The stellar slopes found for the Frontier Fields sample, with median $\gamma_\star = -2.86 \pm 0.05$, are steeper than the ATLAS[3D] stellar slopes of median $\gamma_\star = -2.34 \pm 0.02$. The distribution are shown in Fig. 8. However, as noted in Poci et al. (2017), the stellar profiles become steeper with increasing radius, and so the difference in radial ranges between the two samples becomes critical here. That the stellar slopes are steeper than the total density slopes for both samples is in agreement with simulations, which shows that the total slope is dominated by the stellar profile at small radii and the dark matter profile at large radii (Remus et al. 2013). In addition, the stellar profiles are not well described by a simple power law, but are more curved and thus the power law slopes become increasingly steep for larger fitted radii. In particular, the Magneticum slopes and Frontier Fields stellar slopes extend to larger radii than the ATLAS[3D] slopes, and have correspondingly steeper values. The Magneticum slopes

have a median of $\gamma_\star = -3.06 \pm 0.003$ for the redshift range of the Frontier Fields sample. The profiles cannot be computed across a common radial range due the PSF effects in the inner regions for the Frontier Fields sample, the softening length in the Magneticum simulations which prevents the stellar slopes from being inferred at small radii, and the limited radial extent of the ATLAS[3D] profiles.

The relative spread of the distributions between stellar slopes and total mass density slopes can be used to investigate the so-called bulge-halo conspiracy, where steep light profiles combine with dark matter profiles to form an isothermal total profile (Dutton & Treu 2014). Poci et al. (2017) found that the scatter in the total profiles was only marginally smaller than the stellar profiles for the ATLAS[3D] sample, and as such provided little evidence for a 'conspiracy'. Here, we note that the sensitive dependence of the stellar slopes on the precise radial range used and the limitations of assuming a power law naturally cause the stellar slope values to have larger scatter than the total slope values, which should not be read as evidence towards a bulge-halo conspiracy.

5 DISCUSSION

Assuming that the selected sample of Frontier Fields galaxies is representative of the local ATLAS[3D] sample, the similarity of the density slope distributions indicates there has been no change in the average density slope in the past ~6 Gyr of cosmic time. The consistency of the density slope across this span of time points to an evolutionary process for early-type galaxies that does not significantly perturb the total density slope, such as the dry merging phase described in the two-phase model.

In the two-phase model, galaxies grow in mass through gas-rich accretion events at high redshifts, causing dense central regions and significant rates of star formation. At lower redshifts, relatively frequent gas-poor mergers increase the size of the host galaxy without substantially increasing the mass (Naab et al. 2009; Nipoti, Treu & Bolton 2009; Hilz et al. 2012). The accretion events at large radii also leave the central regions of the host galaxy unperturbed (Karademir et al. 2019). As a consequence, the galaxy 'puffs up', resulting in a shallower total mass density slope. Remus et al. (2013) note that the gas-poor nature of the merger is necessary to drive total mass density slopes towards isothermal values of $\gamma \sim -2$, and that major mergers are also capable of causing this evolution. However, McLure et al. (2013) note that unfeasible rates of major mergers would be required to produce local passive galaxy characteristics from their higher redshift counterparts, and would result in an overpopulation of high-mass stars in the local stellar mass function. McLure et al. (2013) therefore propose a minor-merger evolutionary pathway for passive galaxies, where passive indicates the absence of *in situ* star formation.

It is interesting that dry merger events cause density slopes to approach isothermal values. Remus et al. (2013) argue that approximately isothermal solutions for the total density profile are an 'attractor', as once a galaxy has reached an isothermal density slope, subsequent dry merger events will not change it. Total density slopes might tend towards isothermal solutions due to an incomplete violent relaxation process, such as described by Lynden-Bell (1967). Only merger events with high gas fractions are capable of perturbing isothermal density profiles to steeper values again (Remus et al. 2013). A similar behaviour is seen in the simulations of Nipoti et al. (2009), where dry mergers preserve the isothermal structure of galaxies. The lack of observed density slope evolution between the Frontier Fields sample and ATLAS[3D] sample provides evidence for approximately isothermal density slopes acting as an 'attractor'. This

is consistent with the Magneticum and IllustrisTNG simulations, which show only mild evolution in the total density slope in the past 6 Gyr of cosmic time (Remus et al. 2017; Wang et al. 2019).

The Magneticum simulations quantify the mild evolution in the total density slope with redshift, of the form $\mathrm{d}\gamma/\mathrm{d}z = -0.21z - 2.03$, so that early-type galaxies at higher redshifts have on average steeper slopes (Remus et al. 2017). The IllustrisTNG simulations, with shallower slopes on average, indicate almost no evolution in the density slope below $z \sim 1$ (Wang et al. 2019). In this regard, the fact the ATLAS^{3D} and Frontier Fields density slopes have comparable distributions is more in line with the IllustrisTNG predictions. To further test the correlation between total density slope and redshift as predicted by different simulations, it is necessary to extend the redshift baseline.

A direct, statistical comparison is not made between the Frontier Fields slopes and gravitational lensing slopes, as there are not enough data points within the same redshift range to make a meaningful comparison. However, the lack of evolution with redshift between the Frontier Fields and ATLAS^{3D} samples is in tension with the correlation with redshift of the lensing samples, found by Ruff et al. (2011), Bolton et al. (2012), and Sonnenfeld et al. (2013). Given the lensing trend of shallower density slopes at greater redshifts, Sonnenfeld et al. (2014) argue that there must be continued accretion of modest but non-negligible amounts of gas during dry merger events. The steeper density slopes at low redshift result from the gas condensing in the centre of the galactic potential, leading to small amounts of star formation and denser central regions, with little change to the galactic radius. However, too much cold gas accretion leads to adiabatic contraction and a reduction in effective radius. A contracting radius with redshift is at odds with the expected redshift–size growth of early-type galaxies, which have been shown observationally to increase in agreement with cosmological models (Khochfar & Silk 2006; Trujillo et al. 2007; Huertas-Company et al. 2013; van der Wel et al. 2014). In addition, the ongoing star formation contradicts studies showing early-type galaxies have predominately old and uniform stellar populations (Thomas et al. 2005).

The two-phase model is however consistent with the quiescent stellar populations that characterize early-type galaxies. Stellar populations form in place at early times, with the so-called frosting of younger stars added to the underlying older populations at later times (Trager et al. 2000; Díaz-García et al. 2019). McDermid et al. (2015) found star formation ceased earlier in the Virgo cluster environment compared to the field sample from a star formation history analysis, providing further evidence against ongoing gas accretion at late times in dense environments like that of the Frontier Fields galaxies. Recent studies of galaxy kinematics at high redshifts ($0.6 < z < 1$) also support a dry merger mass build-up scenario for early-type galaxies, restricted to a stable scaling relation between the half-light radius, velocity dispersion, and surface brightness, known as the mass Fundamental Plane (Graaff et al. 2020).

Bolton et al. (2012) instead suggest the importance of off-axis major mergers over continued gas accretion in order to produce the lensing observations of total density slopes that steepen as redshift approaches zero. However, Newman et al. (2012) report the size growth of quiescent galaxies, as measured from observations, is a factor of $\sim$3.5 in the redshift range $0.4 < z < 2.5$, which cannot be explained by the comparatively rare occurrence of major mergers as found by Bundy et al. (2009). Furthermore, Newman et al. (2012) find that dry mergers, with their high growth efficiency, can drive most or all of the observed size growth of quiescent galaxies for $z < 1$.

Gravitational lensing studies at lower redshifts, such as those of Auger et al. (2010), Barnabè et al. (2011), and Shajib et al. (2021),

with samples at $z \sim 0.2$, are consistent with the mean density slopes of this work, with mean density slope measurements of $\langle\gamma\rangle \sim -2.1$. Shajib et al. (2021) suggest the measured slopes from lensing at $z \sim 0.2$, combined with correlations between effective radius and central dark matter fractions, are indicative of dry merging driving the growth of early-type galaxies at low redshifts. It is the lensing measurements of density slopes at higher redshifts ($z \sim 0.6-1$) that indicate shallower mean slopes at greater lookback times.

When comparing the density slope distributions, it is also important to note the differing environments of the Frontier Fields and ATLAS^{3D} galaxies. Some studies indicate that cluster environments accelerate the galaxy evolution process, leading to compact, passive galaxies (Poggianti et al. 2013), although this is debated (Huertas-Company et al. 2013; Shankar et al. 2013). Gallazzi et al. (2021) find massive, passive satellite galaxies in haloes have a systematic excess in their light-weighted stellar ages and metallicities compared to central galaxies, indicating galaxies with older stellar populations prefer high-density regions. At present, there is no clear evidence that environment significantly impacts the density slope measurement.

It is worth noting that the density slopes as predicted by cosmological simulations are derived via a different method from this work. While the Frontier Fields total density slopes are found through dynamical modelling, the simulation slopes are found by co-adding simulation particles within concentric, spherical shells, and fitting with a power law. The impact of the different methods is not yet clear, although Remus et al. (2017) note the discrepancy between gravitational lensing density slopes and those from the Magneticum simulations disappears if lensing techniques are applied to the simulation data. It has, however, been shown that the JAM method is robust for calculating dynamical masses of galaxies, by comparing JAM-derived masses and known masses from simulated galaxies in the Illustris project (Li et al. 2016).

The agreement between the Frontier Fields and ATLAS^{3D} density slope distributions is interpreted as support for the two-phase model of early-type galaxy evolution, with no observed trend of shallower slopes at greater lookback times as found by some lensing works. Extending the study of spatially resolved stellar kinematics to representative samples of higher redshift galaxies, using consistent and homogeneous modelling techniques such as that presented here, is required to resolve the apparent tension in galaxy mass density profiles coming from lensing, dynamics, and simulation predictions.

6 CONCLUSIONS

We present the largest systematic study of two-dimensional stellar kinematic of galaxies at $0.29 < z < 0.55$ to date, using identical general dynamical modelling techniques as employed in large local studies. A sample of 90 galaxies from the Frontier Fields project was analysed using two-dimensional kinematic fields, *HST* photometry, and Jeans dynamical modelling to obtain total mass density slopes in the redshift range $0.29 < z < 0.55$. The main results are as follows:

(i) The median total mass density slope obtained is $\gamma = -2.11 \pm 0.03$ (standard error). The distribution has a standard deviation of 0.23 and a median 1σ uncertainty on each slope of 0.11.

(ii) The obtained density slopes in the Frontier Fields sample agree well with the simulated Magneticum early-type galaxies in the same redshift range. The Frontier Fields density slopes are on average steeper than those of the IllustrisTNG early-type galaxies.

(iii) The distribution of slopes obtained in this work is in agreement with slope distribution in the redshift zero study by Poci et al.

(2017) using ATLAS^{3D} galaxies. The agreement indicates there has been no evolution of the total mass density slope in the last 4–6 Gyr of cosmic time.

(iv) The Magneticum simulations predict a mild evolution in the total density slope in the past 6 Gyr of cosmic time towards shallower slopes. This evolution is not observed when comparing the ATLAS^{3D} and Frontier Fields slope distributions, although pushing to higher redshift will be important to further test this. The lack of evolution in slope is more in agreement with the IllustrisTNG predictions, where the density slope is approximately constant for $z < 1$.

(v) Trends between the total mass density slope and effective radius, velocity dispersion, and surface mass density were investigated. No significant correlation was found with effective radius. However, as for Poci et al. (2017), it was found that galaxies with higher velocity dispersions, and those with higher surface mass densities, have correspondingly steeper slopes. The fact that the found relations are comparable to those found in Poci et al. (2017) indicates similar sample properties and no evolution in the scaling relations.

(vi) The lack of evolution in the density slope is not consistent with observations of density slopes using gravitational lensing methods, which indicate density slopes were shallow at greater lookback times and have become progressively steeper.

The above results place some of the first constraints on the evolution of galaxy density slopes from a consistent application of stellar dynamics to two-dimensional kinematic data, complementing the findings so far only obtainable from gravitational lensing for significant samples. While this reveals elements of agreement and tension with both existing observations and simulations, upcoming developments will help improve the precision of these findings, in particular around the influence of environment, and extend the redshift baseline within which spatially resolved kinematics are available.

New observations of early-type galaxies across a span of redshifts will be aided by the now operational ground-layer adaptive optics system of MUSE, which will alleviate the issue of relatively poor kinematic data quality for intermediate redshifts ($0.2 < z < 0.5$); such an application is the new MAGPI[8] survey (Foster et al. 2021). The MAGPI survey has secured 340 h of MUSE time, to obtain deep, adaptive-optics assisted observations of 160 relatively isolated galaxies at redshifts of $0.25 < z < 0.35$, avoiding the issues of crowding, limited resolution, and low SNR encountered here. The MAGPI survey will help constrain the picture of galaxy evolution in the middle ages of the Universe, and will also help answer questions of the impact of environment on the density slope.

Even further ahead, the *James Webb Space Telescope* will be able to deliver kpc-scale stellar kinematics at $z = 1$ and higher. Planned instruments like MAVIS on the VLT (McDermid et al. 2020; Rigaut et al., in preparation) will be able to provide sub-kpc resolution integral field unit stellar kinematics out to $z = 1$, with HARMONI on E-ELT giving comparable resolution at redshifts beyond 1. Therefore, there will exist a slew of instruments that will deliver high-quality kinematic data, allowing dynamical modelling to probe even higher redshifts.

ACKNOWLEDGEMENTS

DATA AVAILABILITY

Values derived in this work are presented in Table A1. Sources of archival data from which this work is based are given in Section 2.

REFERENCES

Auger M. W., Treu T., Bolton A. S., Gavazzi R., Koopmans L. V. E., Marshall P. J., Moustakas L. A., Burles S., 2010, ApJ, 724, 511
Bacon R. et al., 2010, in McLean I. S., Ramsay S. K., Takami H., eds, Proc. SPIE Conf. Ser. Vol. 7735, Ground-Based and Airborne Instrumentation for Astronomy III. SPIE, Bellingham, p. 773508
Barbary K., 2016, J. Open Source Softw., 1, 58
Barnabè M., Czoske O., Koopmans L. V. E., Treu T., Bolton A. S., 2011, MNRAS, 415, 2215
Barnes J. E., Hernquist L. E., 1991, ApJ, 370, L65
Bellstedt S. et al., 2018, MNRAS, 476, 4543
Bertin E., Arnouts S., 1996, A&AS, 117, 393
Bezanson R. et al., 2018, ApJ, 858, 60
Bezanson R., van Dokkum P. G., Tal T., Marchesini D., Kriek M., Franx M., Coppi P., 2009, ApJ, 697, 1290
Blumenthal G. R., Faber S. M., Primack J. R., Rees M. J., 1984, Nature, 311, 517
Bolton A. S. et al., 2012, ApJ, 757, 82
Brodie J. P. et al., 2014, ApJ, 796, 52
Brownstein J. R. et al., 2011, ApJ, 744, 41
Bundy K. et al., 2014, ApJ, 798, 7
Bundy K., Fukugita M., Ellis R. S., Targett T. A., Belli S., Kodama T., 2009, ApJ, 697, 1369
Caminha G. B. et al., 2017, A&A, 600, A90
Cappellari M. et al., 2007, MNRAS, 379, 418
Cappellari M. et al., 2011, MNRAS, 413, 813
Cappellari M. et al., 2013, MNRAS, 432, 1709
Cappellari M. et al., 2015, ApJ, 804, L21
Cappellari M., 2002, MNRAS, 333, 400
Cappellari M., 2008, MNRAS, 390, 71
Cappellari M., 2017, MNRAS, 466, 798
Cappellari M., Copin Y., 2003, MNRAS, 342, 345
Cappellari M., Emsellem E., 2004, PASP, 116, 138
Coccato L. et al., 2009, MNRAS, 394, 1249
Conselice C. J., 2014, ARA&A, 52, 291
Díaz-García L. A. et al., 2019, A&A, 631, A157
Dutton A. A., Treu T., 2014, MNRAS, 438, 3594
Eichner T. et al., 2013, ApJ, 774, 124
Emsellem E., Monnet G., Bacon R., 1994, A&A, 285, 723
Falcón-Barroso J., Sánchez-Blázquez P., Vazdekis A., Ricciardelli E., Cardiel N., Cenarro A. J., Gorgas J., Peletier R. F., 2011, A&A, 532, A95
Foreman-Mackey D., Hogg D. W., Lang D., Goodman J., 2013, PASP, 125, 306
Foster C. et al., 2021, preprint (arXiv:2011.13567)
Franx M., van Dokkum P. G., Schreiber N. M. F., Wuyts S., Labbe I., Toft S., 2008, ApJ, 688, 770

[8] https://magpisurvey.org

Gallazzi A. R., Pasquali A., Zibetti S., Barbera F. L., 2021, MNRAS, 502, 4457

Graaff A. D. et al., 2020, ApJ, 903, L30

Grillo C. et al., 2015, ApJ, 800, 38

Grillo C. et al., 2016, ApJ, 822, 78

Hilz M., Naab T., Ostriker J. P., 2013, MNRAS, 429, 2924

Hilz M., Naab T., Ostriker J. P., Thomas J., Burkert A., Jesseit R., 2012, MNRAS, 425, 3119

Hogg D. W., Foreman-Mackey D., 2018, ApJS, 236, 11

Huertas-Company M. et al., 2013, MNRAS, 428, 1715

Humphrey P. J., Buote D. A., 2010, MNRAS, 403, 2143

Karademir G. S., Remus R.-S., Burkert A., Dolag K., Hoffmann T. L., Moster B. P., Steinwandel U., Zhang J., 2019, MNRAS, 487, 318

Karman W. et al., 2015, A&A, 574, A11

Khochfar S., Silk J., 2006, ApJ, 648, L21

Koopmans L. V. E., Treu T., 2004, in Plionis M., ed., Astrophysics and Space Science Library, Multiwavelength Cosmology, Vol. 301. Springer Netherlands, Dordrecht, p. 23

Koopmans L. V. E., Treu T., Bolton A. S., Burles S., Moustakas L. A., 2006, ApJ, 649, 599

Lagattuta D. J. et al., 2017, MNRAS, 469, 3946

Larson D. et al., 2011, ApJS, 192, 16

Lauer T. R. et al., 1995, AJ, 110, 2622

Li H., Li R., Mao S., Xu D., Long R. J., Emsellem E., 2016, MNRAS, 455, 3680

Li R. et al., 2019, MNRAS, 490, 2124

Limousin M., Kneib J. P., Bardeau S., Natarajan P., Czoske O., Smail I., Ebeling H., Smith G. P., 2007, A&A, 461, 881

Lotz J. M. et al., 2017, ApJ, 837, 97

Lynden-Bell D., 1967, MNRAS, 136, 101

Mahler G. et al., 2018, MNRAS, 473, 663

Mandelbaum R., van de Ven G., Keeton C. R., 2009, MNRAS, 398, 635

McDermid R. M. et al., 2015, MNRAS, 448, 3484

McDermid R. M. et al., 2020, preprint (arXiv:2009.09242)

McLure R. J. et al., 2013, MNRAS, 428, 1088

Merten J. et al., 2011, MNRAS, 417, 333

Meylan G., Jetzer P., North P., Schneider P., Kochanek C. S., Wambsganss J., 2006, Saas-Fee Advanced Course 33: Gravitational Lensing: Strong, Weak and Micro. Springer-Verlag, Berlin Heidelberg

Mihos J. C., Hernquist L., 1994, ApJ, 431, L9

Monnet G., Bacon R., Emsellem E., 1992, A&A, 253, 366

Mowla L. et al., 2019, ApJ, 880, 57

Naab T., Johansson P. H., Ostriker J. P., 2009, ApJ, 699, L178

Navarro J. F., Frenk C. S., White S. D. M., 1997, ApJ, 490, 493

Newman A. B., Ellis R. S., Bundy K., Treu T., 2012, ApJ, 746, 162

Nipoti C., Treu T., Bolton A. S., 2009, ApJ, 703, 1531

Oogi T., Habe A., 2013, MNRAS, 428, 641

Oser L., Ostriker J. P., Naab T., Johansson P. H., Burkert A., 2010, ApJ, 725, 2312

Peirani S. et al.,2019 MNRAS, 483,4615

Pillepich A. et al., 2018, MNRAS, 473, 4077

Poci A., Cappellari M., McDermid R. M., 2017, MNRAS, 467, 1397

Poggianti B. M., Moretti A., Calvi R., D'Onofrio M., Valentinuzzi T., Fritz J., Renzini A., 2013, ApJ, 777, 125

Remus R.-S., Burkert A., Dolag K., Johansson P. H., Naab T., Oser L., Thomas J., 2013, ApJ, 766, 71

Remus R.-S., Dolag K., Naab T., Burkert A., Hirschmann M., Hoffmann T. L., Johansson P. H., 2017, MNRAS, 464, 3742

Renaud F., Theis C., Boily C. M., 2008, Astron. Nachr., 329, 1050

Richard J., Kneib J.-P., Limousin M., Edge A., Jullo E., 2010, MNRAS, 402, L44

Robertson B., Hernquist L., Cox T. J., Di Matteo T., Hopkins P. F., Martini P., Springel V., 2006, ApJ, 641, 90

Ruff A. J., Gavazzi R., Marshall P. J., Treu T., Auger M. W., Brault F., 2011, ApJ, 727, 96

Salpeter E. E., 1955, ApJ, 121, 161

Sanders D. B., Mirabel I. F., 1996, ARA&A, 34, 749

Scott N. et al., 2013, MNRAS, 432, 1894

Serra P., Oosterloo T., Cappellari M., Heijer M. d., Józsa G. I. G., 2016, MNRAS, 460, 1382

Shajib A. J., Treu T., Birrer S., Sonnenfeld A., 2021, MNRAS, 503, 2380

Shankar F., Marulli F., Bernardi M., Mei S., Meert A., Vikram V., 2013, MNRAS, 428, 109

Sonnenfeld A., Nipoti C., Treu T., 2014, ApJ, 786, 89

Sonnenfeld A., Treu T., Gavazzi R., Suyu S. H., Marshall P. J., Auger M. W., Nipoti C., 2013, ApJ, 777, 98

Springel V. et al., 2018, MNRAS, 475, 676

Teklu A. F., Remus R.-S., Dolag K., Beck A. M., Burkert A., Schmidt A. S., Schulze F., Steinborn L. K., 2015, ApJ, 812, 29

Thomas D., Maraston C., Bender R., Mendes de Oliveira C., 2005, ApJ, 621, 673

Tortorelli L. et al., 2018, MNRAS, 477, 648

Trager S. C., Faber S. M., Worthey G., Gonzalez J. J., 2000, AJ, 120, 165

Treu T., Koopmans L. V. E., 2004, ApJ, 611, 739

Trujillo I., Conselice C. J., Bundy K., Cooper M. C., Eisenhardt P., Ellis R. S., 2007, MNRAS, 382, 109

van de Sande J. et al., 2017, ApJ, 835, 104

van der Wel A. et al., 2014, ApJ, 788, 28

van Dokkum P. G. et al., 2010, ApJ, 709, 1018

Vaughan S. P., Davies R. L., Zielenieski S., Houghton R. C. W., 2018, MNRAS, 479, 2443

Vazdekis A., Sánchez-Blázquez P., Falcón-Barroso J., Cenarro A. J., Beasley M. A., Cardiel N., Gorgas J., Peletier R. F., 2010, MNRAS, 404, 1639

Wang Y. et al., 2019, MNRAS, 490, 5722

Wang Y. et al., 2020, MNRAS, 491, 5188

Weijmans A.-M., Krajnovic D., van de Ven G., Oosterloo T. A., Morganti R., de Zeeuw P. T., 2008, MNRAS, 383, 1343

Weilbacher P. M. et al., 2020, A&A, 641, A28

White S. D. M., Rees M. J., 1978, MNRAS, 183, 341

Whitmore B. C., Schweizer F., 1995, AJ, 109, 960

Williamson R. et al., 2011, ApJ, 738, 139

Wright E. L., 2006, PASP, 118, 1711

Xu D., Springel V., Sluse D., Schneider P., Sonnenfeld A., Nelson D., Vogelsberger M., Hernquist L., 2017, MNRAS, 469, 1824

Zheng W. et al., 2012, Nature, 489, 406

APPENDIX A: GALAXY PARAMETERS

Fig. A1 shows the *HST* MGEs and the MUSE stellar kinematic maps for all 90 galaxies in the sample. The EMCEE posterior distribution for the inner density slope γ' is also shown, along with the modelled $v_{\rm rms}$ fields. Table A1 provides derived values for the galaxies studied in this work, including coordinates, redshifts, stellar density slopes, and total density slopes.
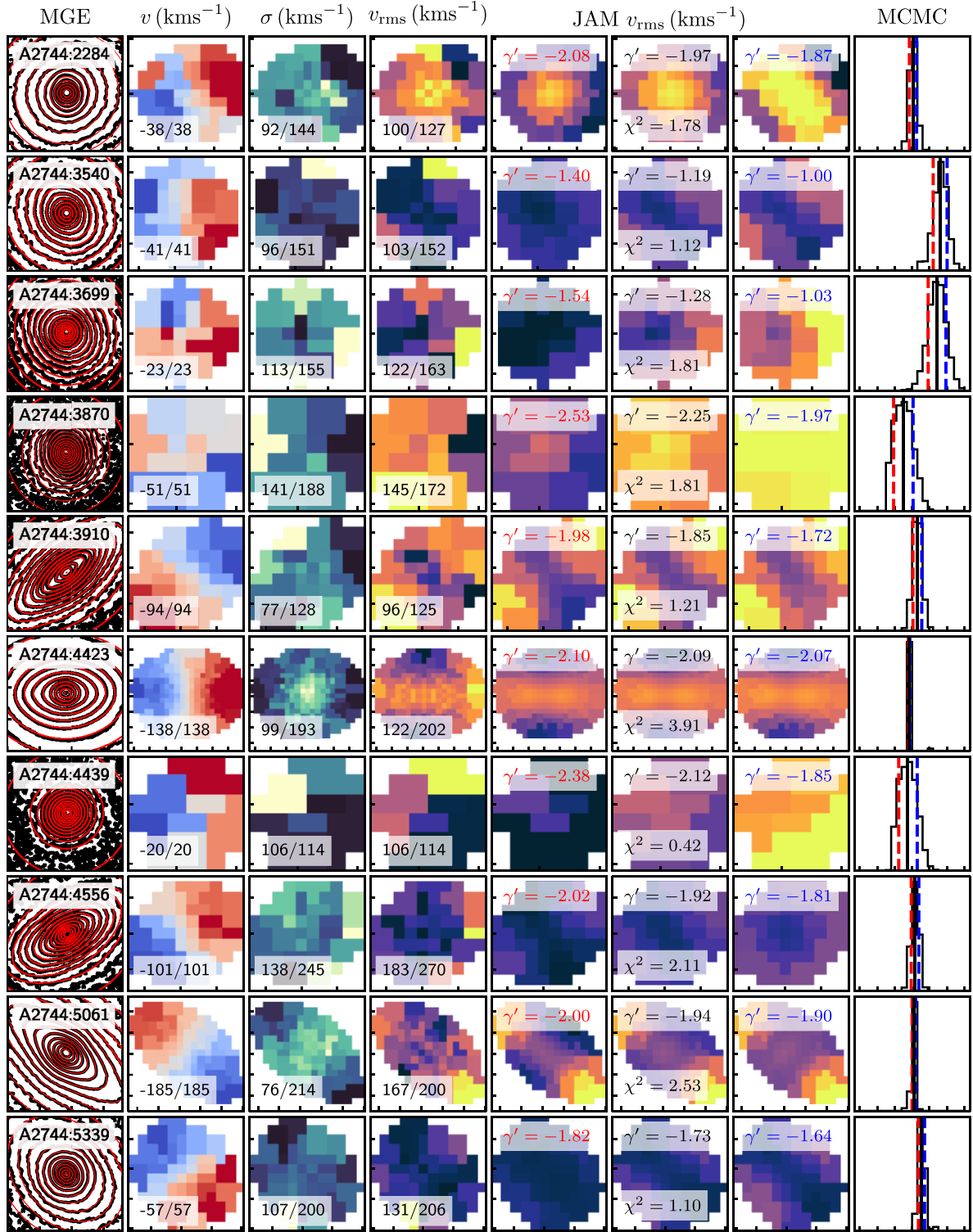
Figure A1. Visual outputs for the 90 galaxies in the sample. Column 1 shows the MGE fit, with the galaxy isophotes in black and the MGE fit in red, in steps of 0.5 mag. The tick marks indicate 0.5 arcsec for the MGE and all kinematic fields. The upper corner of this plot gives the cluster and galaxy ID. Column 2 shows the velocity field from PPXF with the colour scale inset. Column 3 shows the velocity dispersion derived from PPXF. Column 4 shows the observed v_{rms} field, with the colour scale inset. Columns 5, 6, and 7 show the JAM derived v_{rms} fields for the 16th, 50th, and 84th percentile inner density slopes, respectively. The fields are created by taking the relevant percentile of *all* parameters (see Fig. 2). These columns share a common colour scale, and the reduced chi-square value is inset on the median field. Column 8 shows the marginalized distribution of the inner density slopes γ' from EMCEE, with the x-axis spanning -3.5 to -0.5, with tick steps of 0.5. The red and blue dashed lines indicate the 16th and 84th percentiles, respectively, with the median value indicated by a black dashed line.

MGE	$v\,(\mathrm{kms^{-1}})$	$\sigma\,(\mathrm{kms^{-1}})$	$v_{\mathrm{rms}}\,(\mathrm{kms^{-1}})$	JAM $v_{\mathrm{rms}}\,(\mathrm{kms^{-1}})$			MCMC

Figure A1 – *continued*

MGE	$v\,(\mathrm{km\,s^{-1}})$	$\sigma\,(\mathrm{km\,s^{-1}})$	$v_{\mathrm{rms}}\,(\mathrm{km\,s^{-1}})$	JAM $v_{\mathrm{rms}}\,(\mathrm{km\,s^{-1}})$			MCMC
A2744:9283	$-49/49$	$78/107$	$84/97$	$\gamma' = -2.27$	$\gamma' = -2.00$ $\chi^2 = 1.43$	$\gamma' = -1.73$	
A2744:9646	$-27/27$	$104/147$	$104/141$	$\gamma' = -2.08$	$\gamma' = -1.97$ $\chi^2 = 1.23$	$\gamma' = -1.86$	
A2744:9710	$-60/60$	$81/143$	$89/172$	$\gamma' = -1.67$	$\gamma' = -1.54$ $\chi^2 = 1.07$	$\gamma' = -1.41$	
A2744:9876	$-62/62$	$67/90$	$73/91$	$\gamma' = -2.07$	$\gamma' = -1.87$ $\chi^2 = 0.48$	$\gamma' = -1.66$	
A2744:10314	$-97/97$	$98/149$	$125/152$	$\gamma' = -2.28$	$\gamma' = -2.21$ $\chi^2 = 1.40$	$\gamma' = -2.15$	
A2744:10478	$-41/41$	$70/105$	$70/100$	$\gamma' = -2.39$	$\gamma' = -2.29$ $\chi^2 = 1.03$	$\gamma' = -2.18$	
A2744:10689	$-71/71$	$168/291$	$179/292$	$\gamma' = -1.66$	$\gamma' = -1.64$ $\chi^2 = 2.06$	$\gamma' = -1.62$	
A2744:10884	$-64/64$	$99/144$	$116/147$	$\gamma' = -1.86$	$\gamma' = -1.72$ $\chi^2 = 1.02$	$\gamma' = -1.56$	
A2744:11363	$-109/109$	$101/159$	$128/173$	$\gamma' = -2.09$	$\gamma' = -2.02$ $\chi^2 = 1.60$	$\gamma' = -1.94$	
A2744:11418	$-81/81$	$144/215$	$171/207$	$\gamma' = -2.32$	$\gamma' = -2.15$ $\chi^2 = 2.01$	$\gamma' = -1.98$	

Figure A1 – *continued*

Figure A1 – *continued*

MGE	$v\,(\mathrm{km s^{-1}})$	$\sigma\,(\mathrm{km s^{-1}})$	$v_{\rm rms}\,(\mathrm{km s^{-1}})$	JAM $v_{\rm rms}\,(\mathrm{km s^{-1}})$			MCMC
As1063:45	$-126/126$	$191/386$	$219/390$	$\gamma' = -2.05$	$\gamma' = -1.98$ $\chi^2 = 2.15$	$\gamma' = -1.90$	
As1063:51	$-27/27$	$121/157$	$132/143$	$\gamma' = -2.52$	$\gamma' = -2.17$ $\chi^2 = 2.32$	$\gamma' = -1.66$	
As1063:58	$-128/128$	$215/373$	$279/375$	$\gamma' = -2.31$	$\gamma' = -2.18$ $\chi^2 = 1.87$	$\gamma' = -2.07$	
As1063:59	$-72/72$	$162/303$	$182/264$	$\gamma' = -1.54$	$\gamma' = -1.44$ $\chi^2 = 2.27$	$\gamma' = -1.34$	
As1063:78	$-147/147$	$210/406$	$254/408$	$\gamma' = -2.46$	$\gamma' = -2.34$ $\chi^2 = 1.71$	$\gamma' = -2.23$	
As1063:79	$-61/61$	$156/211$	$165/223$	$\gamma' = -1.88$	$\gamma' = -1.70$ $\chi^2 = 0.95$	$\gamma' = -1.53$	
As1063:85	$-44/44$	$184/271$	$206/271$	$\gamma' = -2.16$	$\gamma' = -2.12$ $\chi^2 = 1.80$	$\gamma' = -2.08$	
As1063:87	$-76/76$	$129/222$	$163/214$	$\gamma' = -2.18$	$\gamma' = -1.87$ $\chi^2 = 1.44$	$\gamma' = -1.54$	
As1063:90	$-70/70$	$105/166$	$126/173$	$\gamma' = -1.87$	$\gamma' = -1.64$ $\chi^2 = 1.94$	$\gamma' = -1.39$	
As1063:94	$-76/76$	$113/147$	$132/149$	$\gamma' = -2.32$	$\gamma' = -2.09$ $\chi^2 = 0.47$	$\gamma' = -1.85$	

Figure A1 – *continued*

Figure A1 – *continued*

MGE	v (kms^{-1})	σ (kms^{-1})	$v_{\rm rms}$ (kms^{-1})	JAM $v_{\rm rms}$ (kms^{-1})			MCMC

Figure A1 – *continued*

Figure A1 – *continued*

| MGE | $v\,(\mathrm{km\,s^{-1}})$ | $\sigma\,(\mathrm{km\,s^{-1}})$ | $v_{\mathrm{rms}}\,(\mathrm{km\,s^{-1}})$ | JAM $v_{\mathrm{rms}}\,(\mathrm{km\,s^{-1}})$ | | | MCMC |

Figure A1 – *continued*

Table A1. Derived parameters for the 90 galaxies used in this work. Cluster names are given in redshift order (column 1) with IDs as defined in Section 2 (column 2) and galaxy coordinates given in column 3. Redshifts as found by PPXF using an circular aperture spectrum with the associated aperture velocity dispersions are given in columns 4 and 5. The circularized effective radius of each galaxy is given in column 6, based on the MGE fit. Derived dynamical masses are given in column 7, computed within an effective radius. Stellar density slopes are given in column 8. The stellar density slopes have no associated formal error as they are derived directly from *HST* photometry MGEs, and systematic effects, such as the radial limits used, dominate. The total mass density slopes are given in column 9, with the errors corresponding to the 16th and 84th percentiles of the EMCEE distribution.
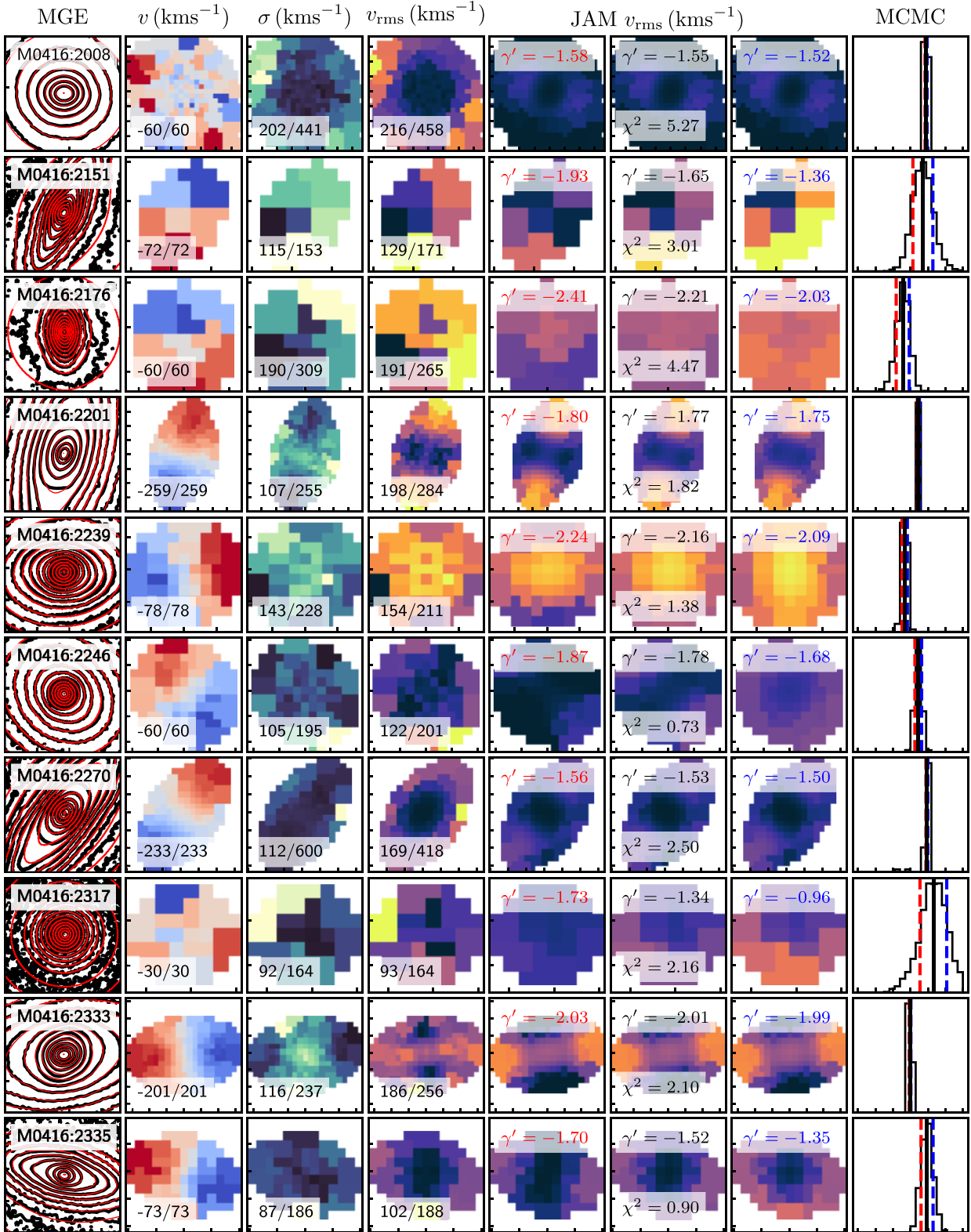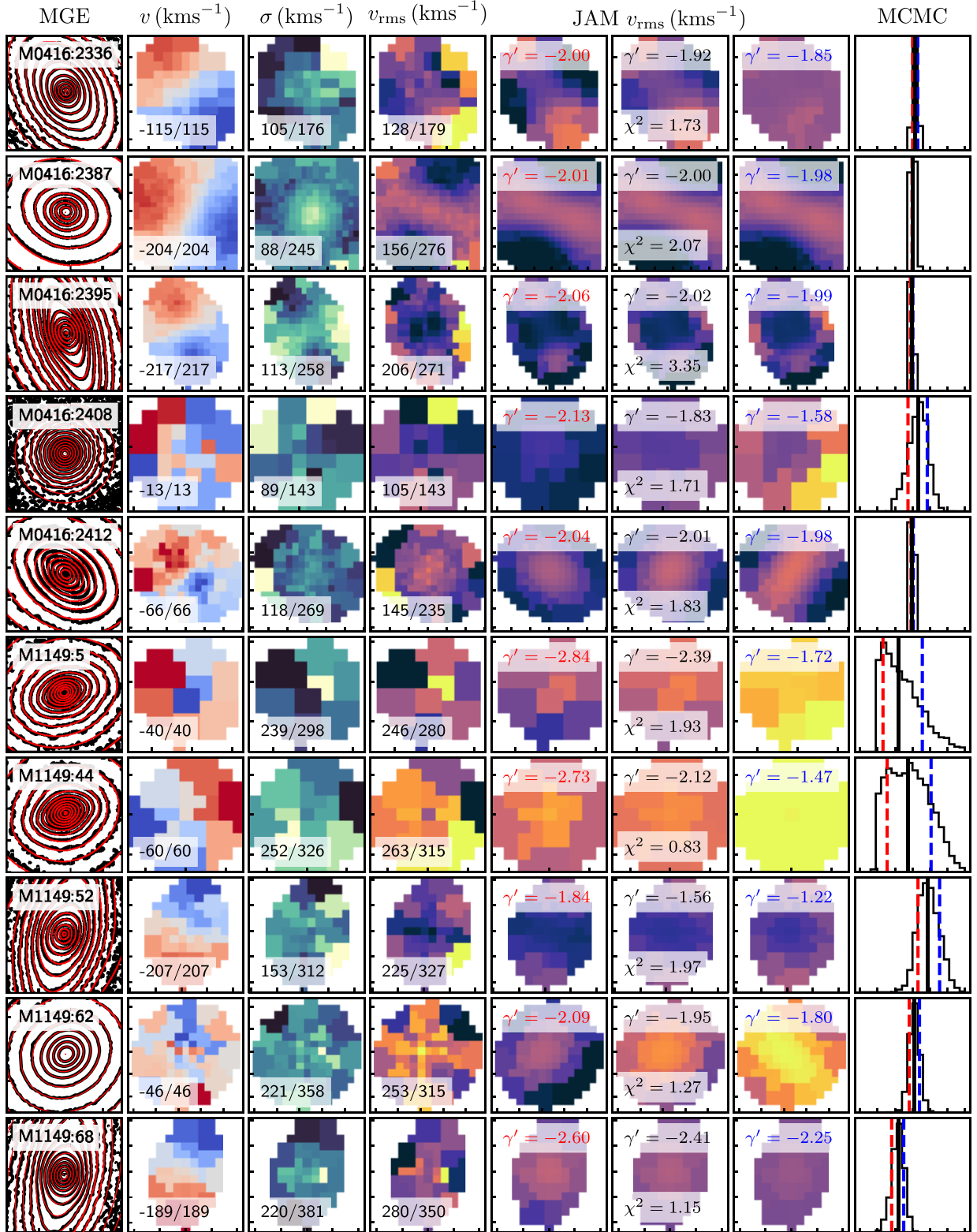
Cluster (1)	ID (2)	Coordinates (J2000) (3)	z (4)	σ_e (kms^{-1}) (5)	R_e (kpc) (6)	$\log_{10}(M/M_\odot)$ (7)	$\gamma_\star$ (8)	γ (9)
A2744	2284	3.602 65, −30.416 96	0.3128	123	1.89	10.56	−2.71	$-2.11^{+0.11}_{-0.10}$
A2744	3540	3.588 82, −30.410 72	0.3218	110	1.73	10.35	−2.76	$-1.39^{+0.21}_{-0.19}$
A2744	3699	3.582 51, −30.409 99	0.3184	130	0.93	10.27	−3.23	$-1.47^{+0.26}_{-0.25}$
A2744	3870	3.595 12, −30.409 37	0.3195	164	1.43	10.66	−3.84	$-2.32^{+0.28}_{-0.28}$
A2744	3910	3.589 13, −30.409 57	0.3171	109	1.32	10.26	−2.67	$-1.99^{+0.13}_{-0.13}$
A2744	4423	3.579 67, −30.409 19	0.3022	188	2.64	10.99	−2.63	$-2.25^{+0.02}_{-0.02}$
A2744	4439	3.590 28, −30.407 40	0.3178	108	2.77	10.57	−4.40	$-2.20^{+0.26}_{-0.27}$
A2744	4556	3.591 72, −30.407 81	0.3189	195	1.42	10.80	−3.19	$-2.05^{+0.11}_{-0.11}$
A2744	5061	3.573 94, −30.408 83	0.3131	183	1.97	10.88	−2.67	$-2.11^{+0.06}_{-0.05}$
A2744	5339	3.595 91, −30.406 21	0.3156	143	2.38	10.75	−2.86	$-1.89^{+0.09}_{-0.09}$
A2744	5693	3.587 04, −30.404 95	0.2983	157	1.45	10.67	−3.59	$-1.84^{+0.12}_{-0.11}$
A2744	6043	3.584 37, −30.402 89	0.3155	87	2.10	10.32	−3.14	$-1.93^{+0.32}_{-0.32}$
A2744	7068	3.605 27, −30.400 81	0.3192	248	0.71	10.73	−3.46	$-2.36^{+0.14}_{-0.12}$
A2744	7229	3.594 46, −30.400 35	0.3031	174	0.79	10.44	−3.47	$-1.98^{+0.17}_{-0.18}$
A2744	7344	3.604 35, −30.400 13	0.3186	163	1.84	10.74	−2.65	$-2.09^{+0.07}_{-0.06}$
A2744	7947	3.593 00, −30.399 33	0.3087	149	1.48	10.58	−2.60	$-2.12^{+0.02}_{-0.02}$
A2744	8067	3.574 91, −30.398 38	0.3171	185	2.52	10.98	−2.46	$-2.21^{+0.06}_{-0.07}$
A2744	8117	3.582 16, −30.398 57	0.2981	168	1.93	10.84	−2.94	$-2.07^{+0.06}_{-0.06}$
A2744	8729	3.578 86, −30.397 12	0.3186	123	2.10	10.56	−2.44	$-2.01^{+0.14}_{-0.12}$
A2744	9072	3.598 96, −30.397 52	0.3157	101	4.98	10.67	−2.26	$-2.17^{+0.07}_{-0.07}$
A2744	9283	3.600 83, −30.394 90	0.3058	92	1.57	10.20	−2.77	$-2.11^{+0.26}_{-0.28}$
A2744	9646	3.578 95, −30.394 12	0.3187	135	2.19	10.68	−2.78	$-2.09^{+0.11}_{-0.11}$
A2744	9710	3.584 98, −30.392 87	0.2951	98	1.11	10.03	−3.01	$-1.71^{+0.12}_{-0.13}$
A2744	9876	3.580 37, −30.392 20	0.2933	81	1.24	9.97	−2.77	$-2.00^{+0.20}_{-0.21}$
A2744	10314	3.590 34, −30.390 94	0.2967	150	1.25	10.53	−3.15	$-2.31^{+0.07}_{-0.07}$
A2744	10478	3.571 50, −30.390 43	0.2960	96	2.63	10.36	−2.57	$-2.38^{+0.10}_{-0.11}$
A2744	10689	3.594 80, −30.391 65	0.3002	218	4.32	11.38	−2.35	$-1.90^{+0.02}_{-0.02}$
A2744	10884	3.590 28, −30.382 69	0.3014	123	1.31	10.37	−2.86	$-1.87^{+0.14}_{-0.16}$
A2744	11363	3.588 15, −30.385 00	0.2972	149	1.27	10.50	−2.78	$-2.15^{+0.07}_{-0.08}$
A2744	11418	3.592 55, −30.385 31	0.3160	200	0.84	10.59	−3.35	$-2.25^{+0.17}_{-0.17}$
A2744	11440	3.605 43, −30.384 84	0.3108	180	1.15	10.68	−3.00	$-2.19^{+0.06}_{-0.06}$
A2744	11856	3.585 31, −30.387 55	0.3002	107	1.72	10.39	−2.57	$-2.31^{+0.04}_{-0.05}$
A2744	11950	3.589 19, −30.387 40	0.3164	195	1.30	10.79	−2.98	$-2.32^{+0.06}_{-0.06}$
A2744	12149	3.598 77, −30.388 02	0.3022	122	1.12	10.33	−3.10	$-1.90^{+0.13}_{-0.14}$
A2744	12269	3.595 51, −30.388 68	0.3027	112	1.48	10.33	−2.91	$-2.11^{+0.18}_{-0.19}$
A2744	12443	3.594 71, −30.389 12	0.3030	95	3.18	10.46	−2.34	$-2.27^{+0.10}_{-0.10}$
As1063	19	342.177 03, −44.536 94	0.3366	136	2.84	10.84	−2.62	$-1.77^{+0.13}_{-0.12}$
As1063	25	342.179 03, −44.532 78	0.3478	292	2.63	11.41	−3.13	$-1.76^{+0.25}_{-0.27}$
As1063	39	342.184 06, −44.526 92	0.3505	133	2.53	10.77	−2.91	$-1.77^{+0.20}_{-0.20}$
As1063	41	342.184 38, −44.536 19	0.3535	157	2.78	10.91	−2.63	$-2.22^{+0.41}_{-0.41}$
As1063	45	342.185 42, −44.518 63	0.3433	263	1.30	11.04	−3.03	$-2.17^{+0.07}_{-0.08}$
As1063	51	342.186 65, −44.522 47	0.3386	140	1.07	10.43	−3.21	$-2.28^{+0.35}_{-0.51}$
As1063	58	342.188 13, −44.525 95	0.3492	306	1.13	11.14	−3.18	$-2.33^{+0.13}_{-0.11}$
As1063	59	342.188 14, −44.529 72	0.3492	198	2.25	11.02	−3.00	$-1.71^{+0.10}_{-0.10}$

Table A1 – *continued*

Cluster (1)	ID (2)	Coordinates (J2000) (3)	z (4)	σ_e (kms^{-1}) (5)	R_e (kpc) (6)	$\log_{10}(M/M_\odot)$ (7)	$\gamma_\star$ (8)	γ (9)
As1063	78	342.193 30, −44.517 82	0.3418	314	0.96	11.12	−3.28	$-2.46^{+0.12}_{-0.11}$
As1063	79	342.193 30, −44.526 43	0.3445	182	1.39	10.72	−3.22	$-1.90^{+0.18}_{-0.17}$
As1063	85	342.195 52, −44.525 99	0.3455	245	2.81	11.32	−2.87	$-2.29^{+0.04}_{-0.04}$
As1063	87	342.197 27, −44.523 27	0.3507	174	1.37	10.72	−3.24	$-2.05^{+0.31}_{-0.33}$
As1063	90	342.200 29, −44.525 20	0.3524	138	2.15	10.64	−2.59	$-1.86^{+0.22}_{-0.25}$
As1063	94	342.204 18, −44.525 24	0.3502	139	1.41	10.53	−2.63	$-2.23^{+0.24}_{-0.23}$
A370	Cl6	39.967 72, −1.586 60	0.3637	178	1.87	10.88	−2.59	$-2.05^{+0.10}_{-0.12}$
A370	Cl12	39.977 45, −1.576 45	0.3676	180	2.40	10.97	−2.53	$-2.12^{+0.10}_{-0.10}$
A370	Cl16	39.971 81, −1.574 78	0.3681	176	1.66	10.74	−2.85	$-2.05^{+0.27}_{-0.25}$
A370	Cl18	39.965 40, −1.586 02	0.3699	212	1.51	10.89	−2.83	$-2.16^{+0.10}_{-0.09}$
A370	Cl19	39.969 60, −1.583 80	0.3702	195	3.74	11.22	−2.62	$-2.12^{+0.04}_{-0.04}$
A370	Cl20	39.970 50, −1.574 88	0.3701	113	3.28	10.66	−2.77	$-1.97^{+0.30}_{-0.29}$
A370	Cl21	39.963 78, −1.581 04	0.3709	244	3.89	11.40	−2.24	$-2.30^{+0.03}_{-0.03}$
A370	Cl24	39.977 26, −1.581 91	0.3710	293	1.38	11.12	−3.00	$-2.37^{+0.09}_{-0.10}$
A370	Cl31	39.968 40, −1.574 69	0.3740	192	3.29	11.09	−2.58	$-2.16^{+0.07}_{-0.07}$
A370	Cl33	39.971 12, −1.586 90	0.3747	204	1.81	10.94	−2.89	$-2.03^{+0.14}_{-0.13}$
A370	Cl35	39.970 60, −1.583 78	0.3754	240	6.76	11.77	−3.01	$-1.75^{+0.14}_{-0.13}$
A370	Cl37	39.975 14, −1.576 87	0.3760	137	1.57	10.59	−3.00	$-2.12^{+0.13}_{-0.13}$
A370	Cl38	39.968 07, −1.575 63	0.3779	157	2.99	10.96	−3.02	$-2.09^{+0.26}_{-0.22}$
A370	Cl46	39.975 79, −1.585 81	0.3806	288	2.10	11.31	−2.92	$-2.21^{+0.04}_{-0.04}$
A370	Cl55	39.969 09, −1.578 69	0.3882	275	2.64	11.39	−2.83	$-2.16^{+0.05}_{-0.06}$
M0416	1843	64.021 98, −24.077 86	0.4054	211	1.33	10.80	−3.46	$-2.49^{+0.21}_{-0.22}$
M0416	1906	64.024 98, −24.072 08	0.3977	246	1.57	11.02	−2.91	$-2.06^{+0.05}_{-0.06}$
M0416	1920	64.025 47, −24.085 09	0.3925	159	2.95	10.84	−2.96	$-2.27^{+0.16}_{-0.14}$
M0416	1975	64.028 31, −24.072 28	0.3926	193	1.87	10.91	−3.12	$-1.64^{+0.12}_{-0.12}$
M0416	2003	64.029 42, −24.079 02	0.4017	139	3.02	10.84	−2.80	$-1.87^{+0.10}_{-0.11}$
M0416	2008	64.029 69, −24.083 44	0.3971	232	6.23	11.66	−2.30	$-1.88^{+0.03}_{-0.03}$
M0416	2151	64.034 74, −24.069 81	0.4011	146	3.84	10.99	−2.71	$-1.82^{+0.28}_{-0.29}$
M0416	2176	64.035 73, −24.069 67	0.3996	241	5.82	11.37	−3.47	$-2.31^{+0.20}_{-0.17}$
M0416	2201	64.036 87, −24.080 66	0.4035	223	3.15	11.25	−2.45	$-2.03^{+0.03}_{-0.03}$
M0416	2239	64.038 23, −24.071 76	0.3958	205	2.40	11.05	−3.07	$-2.28^{+0.08}_{-0.07}$
M0416	2246	64.038 53, −24.062 08	0.4055	128	3.31	10.91	−2.76	$-1.98^{+0.10}_{-0.10}$
M0416	2270	64.039 44, −24.069 32	0.4070	182	2.27	10.90	−2.71	$-1.82^{+0.03}_{-0.03}$
M0416	2317	64.041 82, −24.062 82	0.3953	103	1.32	10.26	−3.53	$-1.54^{+0.39}_{-0.37}$
M0416	2333	64.042 51, −24.069 23	0.3996	221	2.61	11.18	−2.72	$-2.20^{+0.02}_{-0.02}$
M0416	2335	64.042 66, −24.065 14	0.3939	116	3.57	10.71	−2.50	$-1.75^{+0.17}_{-0.17}$
M0416	2336	64.042 76, −24.073 03	0.4060	145	2.20	10.77	−2.82	$-2.11^{+0.07}_{-0.07}$
M0416	2387	64.044 85, −24.073 52	0.4023	221	5.29	11.45	−2.42	$-2.21^{+0.01}_{-0.01}$
M0416	2395	64.045 19, −24.062 13	0.4050	216	2.12	11.05	−3.03	$-2.21^{+0.03}_{-0.03}$
M0416	2408	64.046 12, −24.063 95	0.3976	108	2.06	10.59	−3.96	$-1.97^{+0.30}_{-0.25}$
M0416	2412	64.046 38, −24.067 08	0.3973	189	4.17	11.21	−2.69	$-2.19^{+0.03}_{-0.03}$
M1149	5	177.391 10, 22.404 91	0.5338	259	2.36	11.32	−2.87	$-2.51^{+0.45}_{-0.67}$
M1149	44	177.401 03, 22.397 88	0.5410	306	3.44	11.56	−3.14	$-2.28^{+0.61}_{-0.65}$
M1149	52	177.403 58, 22.396 38	0.5309	257	2.70	11.26	−2.59	$-1.88^{+0.29}_{-0.33}$
M1149	62	177.406 46, 22.389 58	0.5507	290	6.47	11.83	−2.46	$-2.21^{+0.14}_{-0.15}$
M1149	68	177.407 52, 22.403 05	0.5400	315	2.20	11.45	−2.86	$-2.54^{+0.19}_{-0.16}$

APPENDIX B: SIMULATING THE DENSITY SLOPE DEPENDENCE ON DATA QUALITY AND PSF

The salient point of difference between redshift zero studies of total mass density slopes using integral field spectroscopy and this work performed at a higher redshift is the number of spatial elements per kinematic field. This difference can be understood as a result of the cosmological dimming that renders even massive galaxies relatively faint at intermediate redshifts, combined with the reduced angular size of the galaxies at these distances. To determine what impact the number of Voronoi bins has on the derived density slope through the EMCEE process, the MGE of a galaxy with well-defined structural parameters was used to create a simulated kinematic field which was subsequently degraded, with the input and output density slopes compared to ascertain the presence of any bias. Further, since many of the galaxies are close to the PSF resolution of the MUSE instrument, the PSF itself becomes a parameter that has the potential to affect the modelled central mass distribution and density slope, and was also investigated through simple Monte Carlo simulations. The details are as follows.

The underlying photometry of galaxy 4423 in cluster A2744 was chosen to construct the model surface brightness map, as it has a well-fitted MGE and large spatial extent. Additionally, A2744 has three stars in the MUSE field against which the MUSE header FWHM for the PSF can be corroborated, meaning the PSF is particularly well understood for this cluster. The MGE measured on *HST* pixels was resampled on to a coordinate grid with a MUSE pixel scale of 0.2 arcsec, with the surface brightness constructed as an 'apparent' surface brightness in units of magnitudes per square arcsecond.

A polynomial fit to empirical surface brightness and SNR measurements was used to give each pixel of the mock galaxy an SNR. The galaxy was then thresholded to a minimum SNR of 2 per pixel and Voronoi binned to an SNR of 10 per pixel per bin, as was done with the Frontier Fields sample. The best-fitting parameters from the EMCEE models of galaxy 4423 were used to create a total potential model, mapped on to the Voronoi barycentres of the mock galaxy. This total potential model remained fixed for all the simulations. The SNR estimate for each bin was used to create an uncertainty on the v_{rms} value, randomly drawn, in kms^{-1}.

In essence, this process means that by scaling the surface brightness model, the number of kinematic spatial bins can be changed. The reduction in Voronoi bins happens without changing the underlying total potential model, to mimic data quality becoming worse.

A range of mock galaxies, in terms of number of Voronoi bins, were created by scaling the underlying photometry. The mock v_{rms} field was then used to recover the inner density slope using EMCEE in the same way as for the Frontier Field galaxies, described in Section 3.3. Three sets of models were run: those with no scaling to the PSF, those with the PSF overestimated by 33 per cent, and those with the PSF underestimated by 33 per cent. The recovered inner density slope from EMCEE for these simulations are shown in Fig. B1, with the dashed lined indicating the actual inner density slope for all simulations.

With a decreasing number of Voronoi bins, but no uncertainty in the provided PSF, the input density slope was well recovered within the found 1σ uncertainties, with 1σ uncertainties for γ below $\sim$0.2. However, when the number of bins dropped to below $\sim$5,
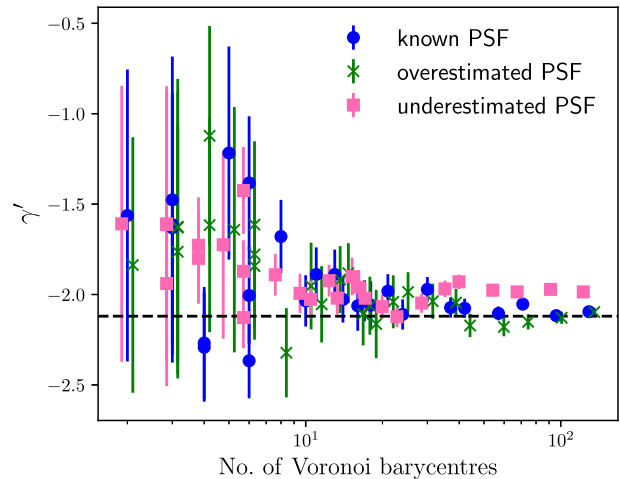
Figure B1. The effect of PSF and degradation of data quality on the recovered density slope is shown. The error bars represent the 16th and 84th percentiles from the obtained EMCEE distribution. The black dashed line shows the input inner density slope value.

the associated errors encompassed the parameter space with no constraint on the density slope (effectively a uniform distribution). No measurable bias was introduced; while the returned density slopes all became shallower for low bin numbers, this is only because the median value of the parameter space was returned. A threshold of at least five bins per kinematic field was used to select the initial galaxy data sample from the MUSE archival data, described in Section 3.1. It should be emphasized here that all data cases where the inner density slope was not constrained within the parameter spaces were excluded, and so the bias towards shallower slopes as a result of data quality seen in these simulations does not affect the results of this work.

For the PSF simulations, a 30 per cent over- and underestimation was used to test the impact of potential (pessimistic) errors on the PSF used. The results of this are shown in Fig. B1. The same lack of constraint for the returned density slope was noted at the level of less than five Voronoi bins. For an overestimated PSF, no bias is apparent in the derived density slopes, and the slopes were again well recovered within the 1σ uncertainties when more than five bins were fitted. However, there is evidence for a mild bias for an underestimated PSF, with estimated uncertainties that do not encompass the input density slope.

While this suggests that an underestimated PSF leads to a modelled field that allows for shallower central regions, the effect was a shift in slope from $\sim$$-2.1$ to $\sim$$-2$. MGE fits to three stars in the Abell 2744 field in comparison to the MUSE header quoted FWHM indicate the error on the FWHM is in fact much smaller than the 33 per cent under or overestimation used in the simulations, on the order of 10 per cent, with a variation across the field of less than 5 per cent. Based on the results of the simulations, it is not expected that the PSF values used in this work on the observed sample artificially shifted the derived density slopes by any significant amount, nor did the use of few spatial elements introduce a bias.

This paper has been typeset from a T$_E$X/L^{A}T$_E$X file prepared by the author.